We are IntechOpen, the world's leading publisher of Open Access books Built by scientists, for scientists

6,900
Open access books available

186,000
International authors and editors

200M
Downloads

Our authors are among the

154
Countries delivered to

TOP 1%
most cited scientists

12.2%
Contributors from top 500 universities

WEB OF SCIENCE™

Selection of our books indexed in the Book Citation Index in Web of Science™ Core Collection (BKCI)

Interested in publishing with us?
Contact book.department@intechopen.com

Numbers displayed above are based on latest data collected.
For more information visit www.intechopen.com

9

Lightwave Refraction and Its Consequences: A Viewpoint of Microscopic Quantum Scatterings by Electric and Magnetic Dipoles

Chungpin Liao, Hsien-Ming Chang, Chien-Jung Liao,
Jun-Lang Chen and Po-Yu Tsai
National Formosa University (NFU)
Advanced Research and Business Laboratory (ARBL)
Chakra Energetics, Ltd.
Taiwan

1. Introduction

In optics, it is well-known that when a visible light beam, e.g., traveling from air (or more strictly, vacuum) into a piece of smooth flat glass at an angle relative to the normal of the air-glass interface, some proportion of the light will be bounced off at the reflection angle equal to the incident angle. However, when the light beam is with its oscillating electric field parallel to the plane-of-incidence (POI, i.e., the plane constituted by both propagation vectors of the incident and reflected light waves, as well as the interface normal vector) (called the p-wave), there is a particular incident angle at which no bounce-off would occur. This particular angle is known as the Brewster angle (θ_B) (Hecht, 2002). In contrast, when the light beam is with its electric field vector perpendicular to the plane-of-incidence (called the s-wave), no such angle exists (Hecht, 2002). In fact, this is only true for uniform, isotropic, and nonmagnetic (or equivalently, with its relative magnetic permeability (μ_r) equal to unity at the optic frequency of interest) materials such as the above glass piece. Indeed, it is known that for magnetic materials, there may instead exist Brewster angles for the s-waves, while none for the p-waves (as will be demonstrated in Section 2).

Traditionally, whichever the case, the Brewster angle is a solid property of the material in question with respect to a given light frequency of interest. Namely, there is a one-to-one correspondence between the Brewster angle and the incident light frequency. However, it is one of the purposes of this chapter to show that the Brewster angle of the material in hand can in principle be modified into a new controllable variable, even dynamically, if a post-process microscopic method called "dipole engineering" is applicable on that material. Among its predictions, the traditionally fixed Brewster angle of a specific material now not only becomes dependent on the density and orientation of incorporated permanent dipoles, but also on the incident light intensity (more precisely, the incident wave electric field strength). Further, two conjugated incident light paths would give rise to different refracted wave powers (Liao et al., 2006).

In order to reveal the intricacies of the mechanism of the proposed permanent dipole engineering subsequently, existing important result of Doyle (Doyle, 1985) is first thoroughly detailed. That is, the Fresnel equations and Brewster angle formula are to be arrived at intuitively and rigorously obtained, by viewing all light-wave-induced dipole moments (including both electric and magnetic dipoles) as the microscopic sources causing the observed macroscopic optical phenomena at an interface, as compared to the traditional academic "Maxwell" approach ignoring the dipole picture. Then, equipped with such-developed intuitive and quantitative physical picture, the readers are then ready to appreciate the way those optically-responsive, permanent dipoles are externally implemented into a selected host matter and their rendered effects. Namely, the Brewster angle of a selected host material becomes alterable, likely at will, and ultimately new optical materials, devices and applications may emerge.

2. Brewster angle and "scattering" form of Fresnel equations

Arising from Maxwell's equations (through assuming linear media and adopting monochromatic plane-waves expansion), Fresnel equations provide almost complete quantitative descriptions about the incident, reflected and transmitted waves at an interface, including information concerning energy distribution and phase variations among them (Hecht, 2002). Two of the Fresnel equations are relevant to reflections associated with both the p and s components (Hecht, 2002):

$$r^s = \frac{E_r^s}{E_i^s} = \frac{n_i \mu_{rt} \cos\theta_i - n_t \mu_{ri} \cos\theta_t}{n_i \mu_{rt} \cos\theta_i + n_t \mu_{ri} \cos\theta_t} \tag{1}$$

$$r^p = \frac{E_r^p}{E_i^p} = \frac{\mu_{ri} n_t \cos\theta_i - \mu_{rt} n_i \cos\theta_t}{\mu_{ri} n_t \cos\theta_i + \mu_{rt} n_i \cos\theta_t} \tag{2}$$

where E is the electric field, μ_r is the relative magnetic permeability, $n = (\varepsilon_r \mu_r)^{1/2}$ is the index of refraction (ε_r being the relative dielectric coefficient), superscripts "p" and "s" stand for the p-wave and s-wave components, while subscripts "i", "r" and "t" denote incident, reflected and transmitted components, respectively. When the incident angle (θ_i) is equal to a particular value (θ_B), one of the above reflection coefficients would vanish, then such value of the incident angle is known as the Brewster angle (θ_B). Note that for the most familiar case in which the light wave is incident from vacuum onto a linear nonmagnetic medium ($\mu_r = 1$), only the p-wave possesses a Brewster angle, not the s-wave.

In the following, to get ready for our proposed idea while without loss of generality, the medium on the incident side is designated to be vacuum (i.e., $n_i = 1$) for simplicity. In addition, to further facilitate our purpose, the Fresnel equations in the equivalent "scattering" form (due to Doyle) are retyped here (Doyle, 1985):

$$\frac{E_t^p}{E_i^p} = \left[\frac{-\sqrt{\mu_r}}{(\mu_r - 1)\sqrt{\varepsilon_r} + (\varepsilon_r - 1)\sqrt{\mu_r} \cos(\theta_t - \theta_i)} \right] \times \left[\frac{2\cos\theta_i \sin(\theta_t - \theta_i)}{\sin\theta_t} \right] \tag{3}$$

$$\frac{E_r^p}{E_i^p}=\left[\frac{(\mu_r-1)\sqrt{\varepsilon_r}-(\varepsilon_r-1)\sqrt{\mu_r}\cos(\theta_t+\theta_i)}{(\mu_r-1)\sqrt{\varepsilon_r}+(\varepsilon_r-1)\sqrt{\mu_r}\cos(\theta_t-\theta_i)}\right]\times\left[\frac{\sin(\theta_t-\theta_i)}{\sin(\theta_t+\theta_i)}\right] \tag{4}$$

$$\frac{E_t^s}{E_i^s}=\left[\frac{-\sqrt{\mu_r}}{(\varepsilon_r-1)\sqrt{\mu_r}+(\mu_r-1)\sqrt{\varepsilon_r}\cos(\theta_t-\theta_i)}\right]\times\left[\frac{2\cos\theta_i\sin(\theta_t-\theta_i)}{\sin\theta_t}\right] \tag{5}$$

$$\frac{E_r^s}{E_i^s}=\left[\frac{(\varepsilon_r-1)\sqrt{\mu_r}-(\mu_r-1)\sqrt{\varepsilon_r}\cos(\theta_t+\theta_i)}{(\varepsilon_r-1)\sqrt{\mu_r}+(\mu_r-1)\sqrt{\varepsilon_r}\cos(\theta_t-\theta_i)}\right]\times\left[\frac{\sin(\theta_t-\theta_i)}{\sin(\theta_t+\theta_i)}\right] \tag{6}$$

Namely, the right hand sides of Eq. (3)-(6) are in the form of D × S, with D being the first bracketed term, representing single dipole (electric and magnetic) oscillation; while S being the second term, depicting the collective scattering pattern generated by the whole array of dipoles. While S is nonzero, where D vanishes (Eq. (4) or (6)) is the condition for the Brewster angle to arise either for the p-wave or the s-wave. That is (Doyle, 1985),

$$\tan^2\theta_B{}^p=\frac{\varepsilon_r(\varepsilon_r-\mu_r)}{\varepsilon_r\mu_r-1} \tag{7}$$

$$\tan^2\theta_B{}^s=\frac{\mu_r(\mu_r-\varepsilon_r)}{\varepsilon_r\mu_r-1} \tag{8}$$

Note that if the medium is characterized by $\mu_r>\varepsilon_r$, only the s-wave may experience the Brewster angle; while in the $\varepsilon_r>\mu_r$ situation, only the p-wave can. Indeed, in the most familiar case of light going from vacuum into a piece of glass whose $\varepsilon_r>\mu_r=1$, there is the Brewster angle only for the p-wave.

In the following, an alternative derivation of the "scattering" form Fresnel equations (Eq. (4)-(6)) will be reproduced from (Doyle, 1985) in somewhat details, which stems from the viewpoint of treating induced microscopic (electric and magnetic) dipoles as the effective sources of macroscopic EM waves at the interface. Then, effective ways to implement the proposed permanent dipoles on a host material will be proposed, which will in principle allow us to achieve variant Brewster angles and thus to create novel materials, devices, even new applications.

3. ''Scattering" form Fresnel equations from the dipole source viewpoint

Microscopically, all matters including optical materials are made of atoms or molecules, each of which further consists of a positive-charged nucleus (or nuclei) and some orbiting

negative-charged electron clouds. When subjected to the EM field of an impinging light wave, the positive and negative charges separate to form induced electric dipoles along the light electric field, while some electrons further move in ways to form induced magnetic dipole moments along the light magnetic field. Note that in this chapter, only far-fields generated by these dipoles are considered and Fig. 1 depicts the relevant orientations.

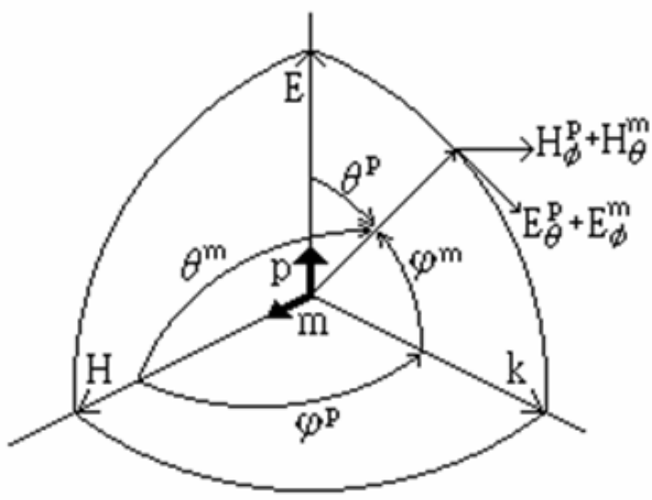

Fig. 1. Orientation of induced dipoles and their fields (Courtesy of W. T. Doyle (Doyle, 1985)).

3.1 The p-wave (E parallel to the plane-of-incidence) case

It is well-known from electromagnetism (Purcell, 1985) that if denoting the induced electric polarization by $\vec{P}$, the electric displacement is: $\vec{D} = \varepsilon_0 \vec{E} + \vec{P}$ for linear isotropic materials. Comparing it with $\vec{D} = \varepsilon_0 \varepsilon_r \vec{E}$, the induced polarization hence emerges as (all in space-time configuration) (Purcell, 1985):

$$\vec{P} = \varepsilon_0 \left(\varepsilon_r - 1 \right) \vec{E}_t^p \tag{9}$$

When calculating the field contribution from the electric dipoles alone, it is assumed that $\mu_r = 1$ and thus $n = \left(\varepsilon_r \right)^{1/2}$. Putting this into an equivalent form of the Snell's law (Doyle, 1985):

$$n^2 - 1 = \frac{\sin\left(\theta_i + \theta_t \right) \sin\left(\theta_i - \theta_t \right)}{\sin^2 \theta_t} \tag{10}$$

and subsequently, together with Eq. (9), into the Fresnel equation relating E_t / E_i, we obtain an expression in which the incident electric field is expressed as a "consequence" of the microscopic sources -- the induced dipoles:

$$E_{ip}^{p} = \left[-\frac{P}{\varepsilon_0} \cos\left(\theta_t - \theta_i \right) \right] \times \left[\frac{\sin \theta_t}{2 \cos \theta_i \sin\left(\theta_t - \theta_i \right)} \right] \tag{11}$$

where the subscript "p" stands for contribution from the induced electric dipoles. Incorporating Eq. (11) into Eq. (2), the reflected electric field manifests itself as due to the electric dipoles sources:

$$E_{rp}^{p}=\left[\frac{P}{\varepsilon_0}\cos\left(\theta_t+\theta_i\right)\right]\times\left[\frac{\sin\theta_t}{2\cos\theta_i\sin\left(\theta_t+\theta_i\right)}\right] \tag{12}$$

Similarly, there are field contributions from the induced magnetic dipoles, which acted through the magnetization $\vec{M}$. Using the magnetic field strength $\vec{H}=\left(\vec{B}/\mu_0\right)-\vec{M}$ and the $E=\frac{\omega}{k}B=v\,B$ relation associated with general monochromatic plane waves, the magnetization becomes (Purcell, 1985):

$$M=\left(\mu_r-1\right)\sqrt{\frac{\varepsilon_0\varepsilon_r}{\mu_0\mu_r}}E_t^p \tag{13}$$

In considering the magnetic contribution, $\varepsilon_r=1$ and thus $n=\left(\mu_r\right)^{1/2}$ are adopted in Eq. (10). Then, using this together with Eq. (13), the Fresnel equation related to E_t/E_i (Eq. (3)), can be converted into an expression for the magnetic component of the incident electric field, in fact as a "consequence" of the microscopic induced magnetic dipoles:

$$E_{im}^{p}=\left[-\frac{M\sqrt{\mu_0}}{\sqrt{\varepsilon_0}}\right]\times\left[\frac{\sin\theta_t}{2\cos\theta_i\sin\left(\theta_t-\theta_i\right)}\right] \tag{14}$$

where the subscript "m" stands for contribution from the induced magnetic dipoles. Putting Eq. (14) into Eq. (2), the magnetic component of the reflected electric field appears as due to the induced magnetic dipoles too:

$$E_{rm}^{p}=\left[-\frac{M\sqrt{\mu_0}}{\sqrt{\varepsilon_0}}\right]\times\left[\frac{\sin\theta_t}{2\cos\theta_i\sin\left(\theta_t+\theta_i\right)}\right] \tag{15}$$

When a light wave impinges on an interface, it causes the excitation of electric and magnetic dipoles throughout the second medium, which in turn collectively give rise to reflected, transmitted, and formally, incident waves at the interface. As depicted in Fig. 1, as long as far fields are concerned, the induced electric and magnetic dipoles can be viewed as aligned along the incident electric and magnetic field vectors, respectively. All electric and magnetic fields of interface-relevant waves can be conceived as generated by the co-work of electric and magnetic dipoles. (Of course, for the incident wave, this is only formally true, that is, the incident fields are the "cause" not the "effect" of dipole oscillations.) We thus write:

$$E_i^p=E_{ip}^p+E_{im}^p \tag{16}$$

Namely, by adding Eq. (11) and (14), the incident electric field can be formally expressed as due to induced dipole sources P and M :

$$E_i^p = \left[-\frac{P}{\varepsilon_0}\cos\left(\theta_t - \theta_i\right) - \frac{M\sqrt{\mu_0}}{\sqrt{\varepsilon_0}} \right] \times \left(\frac{\sin\theta_t}{2\cos\theta_i \sin\left(\theta_t - \theta_i\right)} \right) \tag{17}$$

As a verification, if putting forms of these sources (i.e., Eq. (9) and (13) in which the induced P and M are expressed in term of E_t^p) back into Eq. (17), it is found that the obtained transmission coefficient of the p-wave is exactly that of Eq. (3).

Similarly, conceiving the reflected electric field as:

$$E_r^p = E_{rp}^p + E_{rm}^p \tag{18}$$

Adding Eq. (12) and (15), the reflected electric field appears as due to the induced dipole sources P and M :

$$E_r^p = \left[\frac{P}{\varepsilon_0}\cos\left(\theta_t + \theta_i\right) - \frac{M\sqrt{\mu_0}}{\sqrt{\varepsilon_0}} \right] \times \left(\frac{\sin\theta_t}{2\cos\theta_i \sin\left(\theta_t + \theta_i\right)} \right) \tag{19}$$

Similarly, putting forms of the dipoles sources (i.e., Eq. (9) and (13) in which P and M are expressed in terms of E_t^p) back into Eq. (19), and using the newly obtained E_i^p vs. E_t^p relation (i.e., Eq. (17)), it is found that the obtained reflection coefficient of the p-wave is exactly that of Eq. (4), in "scattering" form.

3.2 The s-wave (E perpendicular to the plane-of-incidence) case

Likewise, following Fig. 1 again, we can also express the incident and reflected electric fields of the s-wave as due to those induced electric and magnetic dipoles:

$$E_i^s = \left(-\frac{P}{\varepsilon_0} - \frac{M\sqrt{\mu_0}}{\sqrt{\varepsilon_0}}\cos\left(\theta_t - \theta_i\right) \right) \times \left(\frac{\sin\theta_t}{2\cos\theta_i \sin\left(\theta_t - \theta_i\right)} \right) \tag{20}$$

$$E_r^s = \left(-\frac{P}{\varepsilon_0} + \frac{M\sqrt{\mu_0}}{\sqrt{\varepsilon_0}}\cos\left(\theta_t + \theta_i\right) \right) \times \left(\frac{\sin\theta_t}{2\cos\theta_i \sin\left(\theta_t + \theta_i\right)} \right) \tag{21}$$

and that the transmission and reflection coefficients are indeed found to be those of Eq. (5) and (6), respectively, in "scattering" form.

4. The proposed permanent dipoles engineering

4.1 Observations and inspirations

From the above elaboration, it becomes obvious that the electric and magnetic dipoles can be much more than mere pedagogical tools for picturing dielectrics and magnetics, as indeed proven by Doyle (Doyle, 1985). In fact, treating them as microscopic EM wave sources from the outset, the "scattering" form of Fresnel equations (i.e., Eq. (3)-(6)), and consequently, the Brewster angle formulas (Eq. (7) and (8)) can all be reproduced. Then, emerging from such

details come our inspired purposes. Namely, by acquainting ourselves with the role played by these *induced* dipoles (or, the microscopic scattering sources), it is then intuitively straightforward to learn how new macroscopic optical phenomena, such as the new Brewster angle may be generated if extra anisotropic optically-responsive *permanent* dipoles were implemented onto the originally isotropic host material in discussion (Liao et al., 2006). In other words, now the notions of P and M are further extended to include the total effects resulting from both the *induced* and *permanent* dipoles.

For instance, in Eq. (17), the $\cos(\theta_t - \theta_i)$ factor multiplying on P (but not on M) is due to the fact that the induced polarization P (along E_t^p) has only a fractional contribution to E_i^p determined by the vector projection as shown in Fig. 2, for the p-wave situation. Now, if an external polarization vector $P_0(\omega)$ (as the collective result of many imposed electric dipoles responding to the incident lightwave of radian frequency ω at the incident angle θ_i) is introduced within a host material, then, e.g., for the p-wave case, all electric dipoles' contribution to E_i^p (i.e., Eq. (17)) is now $P_{induced}\cos(\theta_i - \theta_t) + P_0\cos(\theta_0 + \theta_i)$, or $\varepsilon_0(\varepsilon_r - 1)E_t^p\cos(\theta_i - \theta_t) + P_0\cos(\theta_0 + \theta_i)$ (see Fig. 2). Namely, there is now an additional second anisotropic term resulting from *externally* imposed dipoles whose contribution may not necessarily be less than the induced dipoles of the original isotropic host. Note that the incident light-driven response of these externally imposed permanent dipoles is frequency dependent, and therefore, the above P_0 really stands for that amount of polarization at the relevant optical frequency of interest and the lightwave's incident angle θ_i. In other words, a "DC" polarization will never enter the above equation, and P_0/E_t^p would be constant for each specific θ_i if the added dipoles, and hence the resultant polarization, are linear.

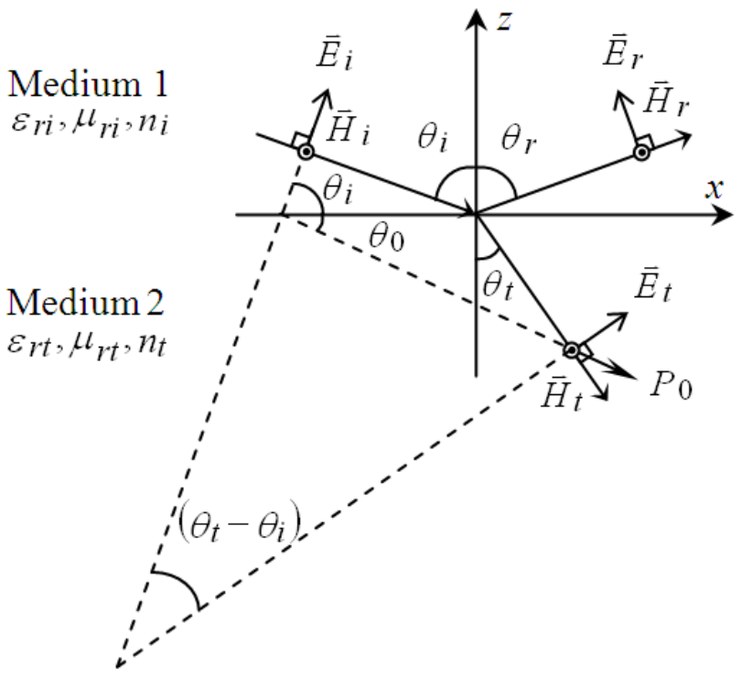

Fig. 2. P-wave configuration at the interface and the orientation of embedded permanent electric dipoles (Courtesy of W. T. Doyle (Doyle, 1985)).

Thus, if the dipole-engineered total contribution is recast in the traditional form, viz., $\varepsilon_0(\tilde{\varepsilon}_r - 1)E_t^p \cos(\theta_i - \theta_t)$, then it is clear that the modified relative dielectric coefficient is equivalently (Liao et al., 2006):

$$\tilde{\varepsilon}_r = \frac{P_0}{\varepsilon_0 E_t^p} \frac{\cos(\theta_i + \theta_0)}{\cos(\theta_i - \theta_t)} + \varepsilon_r \tag{22}$$

where θ_0 is the angle between the imposed extra polarization vector and the interface plane (see Fig. 2). Thus, by putting Eq. (22) into the p-wave Brewster angle formula (Eq. (7)), a new Brewster angle (θ_B) would then emerge:

$$\tan^2 \theta_B{}^p = \frac{\tilde{\varepsilon}_r(\tilde{\varepsilon}_r - \mu_r)}{\tilde{\varepsilon}_r \mu_r - 1} \tag{23}$$

4.2 Justification of the effectiveness and meaningfulness of implementing optically-responsive dipoles

A justification of the effectiveness of the proposed *permanent* dipole engineering is straightforward by noting the following fact. Namely, had the original host material been transformed into a new material by adding in a considerable amount of certain second substance, then P_0 in the above really would have stood for the extra induced dipole effect resulting from this second substance.

However, to this end, an inquiry may naturally arise as to whether the outcome of the proposed dipole-engineering approach being nothing more than having a material of multi-components from the outset. The answer is clearly no, and there are much more meaningful and practical intentions behind the proposed method. First of all, this is a controllable way to make new materials from known materials without having to largely mess around with typically complicated details of manufacturing processes pertaining to each involved material (if the introduced *permanent* dipoles are noble enough). Indeed, we have been routinely attempting to create various materials by combining multiple substances, and yet have also been very much limited by problems related to chemical compatibility, phase transition, in addition to many processing and economic considerations. Secondly, *permanent* dipole engineering would further allow delicate, precise means of manipulating the material properties, such as varying the dipole orientation to render desired optical performance on host materials of choice. Thirdly, all existing techniques known to influence dipoles can be readily applied on the now embedded dipoles to harvest new optical advantages, such as by electrically biasing the dipoles to adjust the magnitude of *permanent* dipole moment (in terms of P_0) in the frequency range of interest.

4.3 Different refracted wave powers on two conjugated incident light paths

If, instead of picking the incidence from the left hand side as depicted in Fig. 2, a conjugate path, i.e., from the right hand side, is taken (see, Fig. 3), then the formula for Eq. (22) becomes (Liao et al., 2006):

$$\tilde{\varepsilon}_r = \frac{P_0}{\varepsilon_0 E_t^p} \frac{\cos(\theta_i - \theta_0)}{\cos(\theta_t - \theta_i)} + \varepsilon_r \tag{24}$$

Unconventional Brewster angle can be found by Eq. (23) (p-wave case).

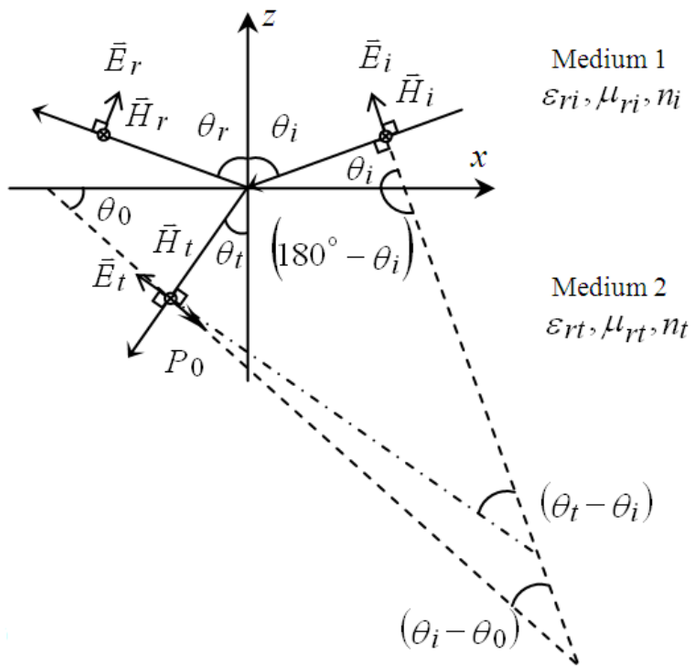

Fig. 3. P-wave configuration and the orientation of embedded permanent electric dipoles (Conjugated Incident Light Path, courtesy of W. T. Doyle (Doyle, 1985)).

In other words, the traditionally fixed Brewster angle of a specific material now not only becomes dependent on the density and orientation of incorporated permanent dipoles, but also on the incident light intensity (more precisely, the incident wave electric field strength). Further, two conjugated incident light paths would give rise to different refracted wave powers (Liao et al., 2006), (Haus & Melcher, 1989).

4.4 The surface embedded with a thin distributed double layer

The traditional Fresnel equations in the electromagnetic theory have been used in determining the light power distribution at an interface joining two different media in general. They are known to base upon the so-called "no-jump conditions" ((Haus & Melcher, 1989), (Hecht, 2002)) wherein the interface-parallel components of the electric and magnetic fields of a plane wave continue seamlessly across the interface, respectively:

$$\langle E_{||} \rangle = 0 \quad and \quad \langle H_{||} \rangle = 0 \tag{25}$$

where $\langle Q \rangle \equiv Q_a - Q_b$ stands for the discontinuity of the physical quantity Q by crossing from the a side to the b side of the interface, and $||$ (or $\perp$) is with respect to the interface plane. The general configuration of light incidence can be decomposed into the p-wave and s-wave situations. For the p-wave case, the lightwave's electric field is on the plane of incidence (POI) (see Fig. 4), and for the s-wave situation, it is pointing perpendicularly out of the POI.

When a light beam of frequency ω is incident from air (*a* side) onto a flat smooth dielectric (*b* side) embedded with a layer of distributed, incident-light-responsive electric dipoles near the surface (see Fig. 5), the above jump condition for the electric field becomes (Haus & Melcher, 1989):

$$E_{||}{}^{a} - E_{||}{}^{b} \equiv \left\langle E_{||} \right\rangle = -\frac{1}{\varepsilon_0}\frac{\partial \pi_s}{\partial x} \tag{26}$$

where ε_0 is the dielectric permittivity of free space. An interfacial double layer is composed of a top and bottom layers of equal but opposite surface charges ($\pm\sigma_s$) respectively and separated by a tiny distance (d). It is mathematically described by $\sigma_s \to \infty$ and $d \to 0$ such that $\pi_s \equiv \sigma_s \cdot d$ stands for the electric dipole moment per unit area on the interface. Eq. (26) is obtained through integrating Faraday's law $\nabla \times \vec{E} = -\partial\, \mu \vec{H} / \partial t$ (μ being the magnetic permeability) over a vanishingly thin strip area enclosing a section of the interface on the plane of incidence (see Fig. 5). Thus, with the integration on the right hand side being null, further applying Stokes' theorem ((Haus & Melcher, 1989), (Hecht, 2002)) on the left hand side reveals that the two normal sections (i.e., along $\vec{E}_{\perp}$) in the contour integration no longer cancel each other. This is because the vertical electric field distribution is now non-uniform in the presence of a distributed double layer (see Fig. 5). Thus, instead of continuing across smoothly, the jump in $E_{||}$ is now proportional to the spatial derivative of the electric dipole moment per unit area (π_s) on the interface, which in general is a space-time variable, i.e., $S(\vec{r},t)$ (Chen et al., 2008). In other words,

$$\begin{aligned} &\left\langle E_{||} \right\rangle \equiv E_{||}{}^{a} - E_{||}{}^{b} = \left(E_{i||} + E_{r||}\right) - E_{t||} = \\ &-\frac{1}{\varepsilon_0}\frac{\partial \pi_s}{\partial x}(t) \equiv S(\vec{r},t) \; = S_M(t)\cos\left(\vec{k}_s \cdot \vec{r} - \omega_s t\right) \end{aligned} \tag{27}$$

where the subscripts "i", "r", and "t" represent the incident, reflected, and transmitted components, respectively. In other words, the condition $\left\langle E_{||} \right\rangle \neq 0$ arises where there is non-uniform distribution of the dipole moment along the projection of the incident light's electric field on the interface. That is, the nonzero $E_{||}$ jump is effectively proportional to the displacement of a longitudinal (σ_s varying) or transverse (d varying) mechanical wave $S(t)$, which is excited by the incident wave and propagating along the double layer with wave vector $\vec{k}_s$ and frequency ω_s. Further, such a mechanical wave can additionally be modulated transversely in its dipole length (i.e., d) by a second wave of frequency ω_M such that $S_M(t) = S_{x0}\cos\omega_M t$ for the p-wave case, and $S_M(t) = S_{y0}\cos\omega_M t$ for the s-wave case. In the above, the modulating wave amplitudes are $S_{x0} = -\frac{1}{\varepsilon_0}\left(\frac{\partial \pi_s}{\partial x}\right)_0$ and $S_{y0} = -\frac{1}{\varepsilon_0}\left(\frac{\partial \pi_s}{\partial y}\right)_0$, respectively, with the subscript "0" standing for the root-mean-square amplitude.

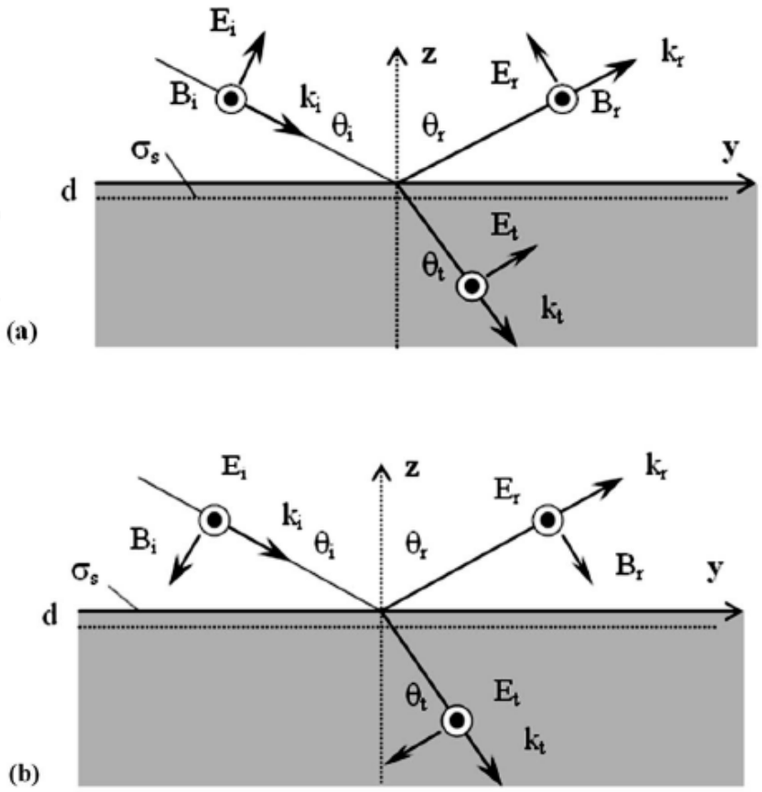

Fig. 4. (a) Refraction with p-wave incidence and (b) refraction with s-wave incidence.

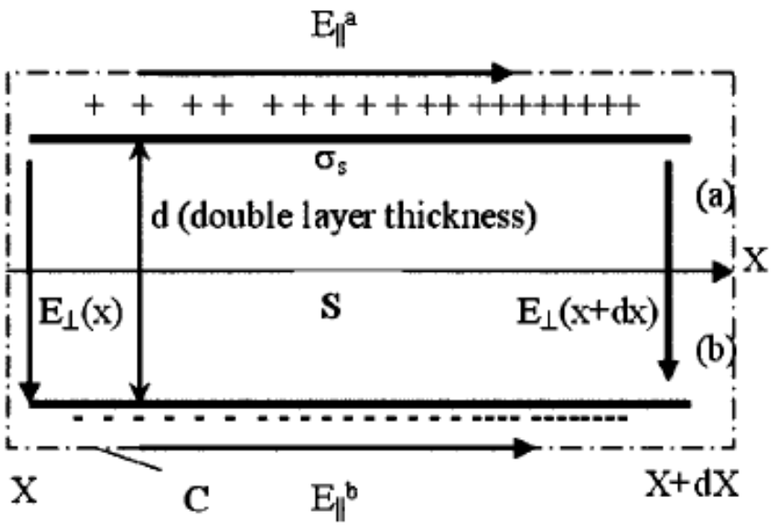

Fig. 5. Surface integration of Faraday's law enclosing a section of the double layer and regions above (a) and below (b) it.

By combining with the other jump condition, i.e., $\left\langle H_{||} \right\rangle = 0$, the modified Fresnel reflection coefficient for both the p- and s-wave configurations emerge readily after some algebraic manipulations (Chen et al., 2008):

$$r_p \equiv \left(\frac{E_{r0}}{E_{i0}}\right)_p = \frac{\overbrace{\left(\frac{n_t}{\mu_t}\cos\theta_i - \frac{n_i}{\mu_i}\cos\theta_t\right)}^{traditional}}{\left(\frac{n_t}{\mu_t}\cos\theta_i + \frac{n_i}{\mu_i}\cos\theta_t\right)} - \underbrace{\frac{\frac{n_t}{\mu_t}S_{y0}\cos\omega_M t}{\left(\frac{n_t}{\mu_t}\cos\theta_i + \frac{n_i}{\mu_i}\cos\theta_t\right)E_{i0}}}_{due\ to\ distributed\ double\ layer} \tag{28}$$

$$r_s \equiv \left(\frac{E_{r0}}{E_{i0}}\right)_s = \frac{\overbrace{\left(\frac{n_i}{\mu_i}\cos\theta_i - \frac{n_t}{\mu_t}\cos\theta_t\right)}^{traditional}}{\left(\frac{n_i}{\mu_i}\cos\theta_i + \frac{n_t}{\mu_t}\cos\theta_t\right)} + \underbrace{\frac{\frac{n_t}{\mu_t}S_{x0}\cos\omega_M t\cdot\cos\theta_t}{\left(\frac{n_i}{\mu_i}\cos\theta_i + \frac{n_t}{\mu_t}\cos\theta_t\right)E_{i0}}}_{due\ to\ distributed\ double\ layer} \tag{29}$$

The new power reflection coefficient is then $R = r^2$ and the new power transmission coefficient is: $T = 1 - R$, for both the p- and s-wave cases (Hecht, 2002). Therefore, in the presence of a light-responsive, distributed double layer at the interface (e.g., with $\partial\pi_s/\partial x > 0$ or $\partial\pi_s/\partial y > 0$ in Fig. 4), the reflected and transmitted lights are expected to be further modulated at the frequency ω_M. Additionally, this modification to the light reflectivity is incident-power-dependent. Namely, variation in reflectivity is more significant for dimmer incident lights, as implied by the presence of E_{i0} in the denominator of the 2nd term in both Eqs. (28) and (29). Note that these seemingly peculiar behaviors are by no means related to the well-known photoelectric effects, such as those manifested by light-guiding molecules used in liquid crystal displays.

In the absence of the second modulating light, the $\cos\omega_M t$ factor is reduced to unity in both Eqs. (28) and (29). As a consequence, the modified light reflection is no longer time-varying, but is either enhanced or decreased depending on the signs of S_{x0} or S_{y0} in the p- and s-polarized cases, respectively. More importantly, asymmetric reflection (or, refraction) would result should the path leading from the incidence to the reflection be reversed (see, e.g., Fig. 4), as the result of a sign change of the corresponding coordinate system. In the following, experimental investigations are conducted on the above-predicted power reflection asymmetry between conjugate light paths, as well as on the inverse dependence of reflectivity upon the incident power.

5. Possible implementations of altered Brewster angle demonstrated by quantum mechanical simulations

Numerical experiments for the p-wave case were conducted as an example to evidence the variation of Brewster angles rendered by the proposed dipole engineering. This task very

much relied on the first-principle quantum mechanical software: CASTEP (Clark et al., 2005). CASTEP is an *ab initio* quantum mechanical program employing density functional theory (DFT) to simulate the properties of solids, interfaces, and surfaces for a wide range of materials classes including ceramics, semiconductors, and metals. Its first-principle calculations allow researchers to investigate the nature and origin of the electronic, optical, and structural properties of a system without the need for any experimental input other than the atomic number of mass of the constituent atoms.

The adopted simulation procedure was as follows (Liao et al., 2006). CASTEP first simulated the spectral dependence of the relative dielectric coefficient (ε_r , including the real (ε_{rR}) and imaginary (ε_{rI}) parts) of a chosen host material. Then, dipole engineering was exercised on this host lattice through artificially replacing some of its atoms with other elements, or with vacancy defects, hence resulting in the implementation of permanent dipoles of known orientation (θ_0) on the host. Due to this introduced anisotropy, we had to simulate the corresponding spectral dependence of the new relative dielectric coefficient ($\tilde{\varepsilon}_r$) for each incident angle (θ_i). Namely, $\tilde{\varepsilon}_r$ was then θ_i -dependent. Using the new medium refractive index ($n_t \approx \sqrt{\varepsilon_{rR}}$ for low ε_{rI} case; otherwise, $n_t = \sqrt{{\varepsilon_{rR}}^2 + {\varepsilon_{rI}}^2} \cdot \cos(\varphi/2)$ where $\tan(\varphi/2) = -\varepsilon_{rI}/\varepsilon_{rR}$ has to be used) and Snell's law, the corresponding refractive angle (θ_t) could thus be secured. (However, since CASTEP only simulates intrinsically, viz., it does not do Snell's law, we actually had to vary θ_t first instead and went backward to secure θ_i using Snell's law.) Then, using Eq. (22), the value of such-introduced permanent polarization at the incident angle θ_i, in terms of $P_0 \Big/ \left(\varepsilon_0 E_t^p\right)$ at θ_i, was revealed. The resultant new Brewster angle was thus obtained through inspecting the modified reflection coefficient (i.e., Eq. (2), with ε_r replaced by ε_{rR}, and $n_i = 1$, and $\mu_{ri} = \mu_{rt} = 1$, becomes $r^p = \left(\sqrt{\tilde{\varepsilon}_{rR}}\cos\theta_i - \cos\theta_t\right) \Big/ \left(\sqrt{\tilde{\varepsilon}_{rR}}\cos\theta_i + \cos\theta_t\right)$) curve against θ_i varying from 0 to 90 degrees.

Two example situations are given here, where dipole engineering can noticeably alter the Brewster angles of a single-crystal silicon wafer under the incidence of a red and an infrared light, respectively (Liao et al., 2006). The red light is of energy 1.98 eV, or, vacuum wavelength λ = 0.63 μm. The infrared light is of energy 0.825 eV, or, λ = 1.5 μm. It is well-known that without the proposed dipole engineering treatment, the single-crystal silicon is opaque to the visible (red) light, while fairly transparent to the infrared light. In fact, for the latter reason, infrared light is routinely applied in the front-to-back side pattern alignment of wafers in microelectronic fabrications.

Here the Si single-crystal unit cell is modified by replacing 2 of its 8 atoms with vacancies (see Fig. 6, regions in dim color are the chopped-out sites). Note that the x-axis corresponds to $\theta_t = 0^\circ$ (and hence $\theta_i = 0^\circ$), while y or z-axis to $\theta_t = 90^\circ$. Fig. 6 shows that the defect-caused permanent polarization (maximum P_0) is most likely along the x-direction. The CASTEP-simulated curves of $\tilde{\varepsilon}_r$ vs. light energy (in eV) in the incident directions of x, y, and z, respectively, are given in Fig. 7. Hence, $\tilde{\varepsilon}_r$ is, as expected, θ_i -dependent. For both cases in which the incident light is red and infrared, the involvement of the introduced

optically-responsive defect polarization is very much dependent on the its relative orientation with respect to the refractive p-wave's electric field (E_t^p) (see Figs. 8 and 9). Indeed, as evident from Fig. 2, it is most significant when E_t^p is in the direction of the permanent polarization (maximum P_0).

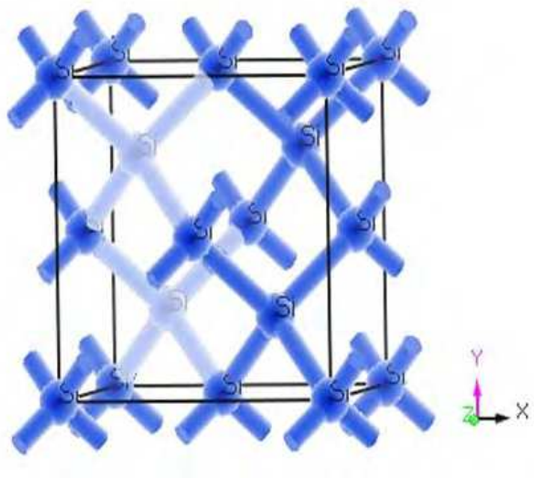

Fig. 6. Unit cell of the modified Si crystal with two vacancies (Space group: FD-3M (227); Lattice parameters: a: 5.43, b: 5.43, c: 5.43; α: 90°, β: 90°, γ: 90°).

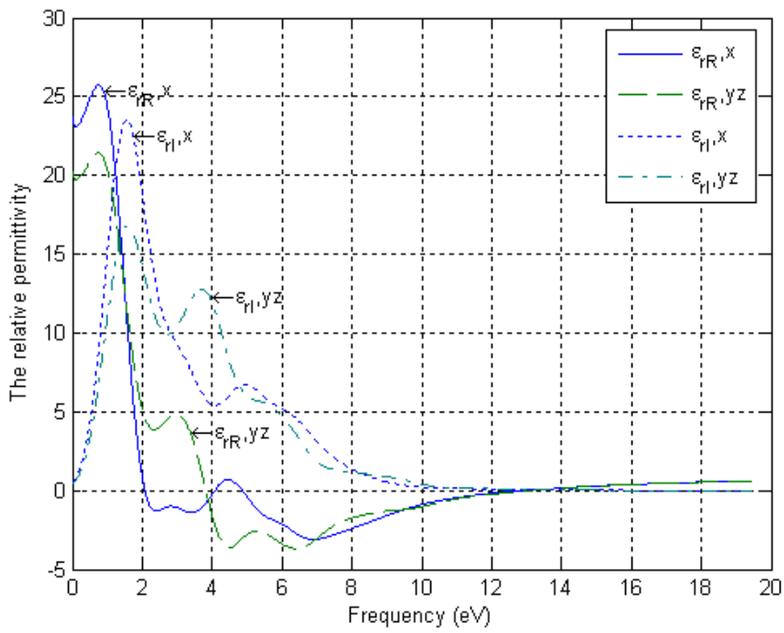

Fig. 7. The modified relative dielectric coefficient spectra ($\tilde{\varepsilon}_r = \tilde{\varepsilon}_{rR} + i\tilde{\varepsilon}_{rI}$), with the refractive light's propagation directions shown for x, y, and z axes, for $\theta_0 = 0^\circ$.

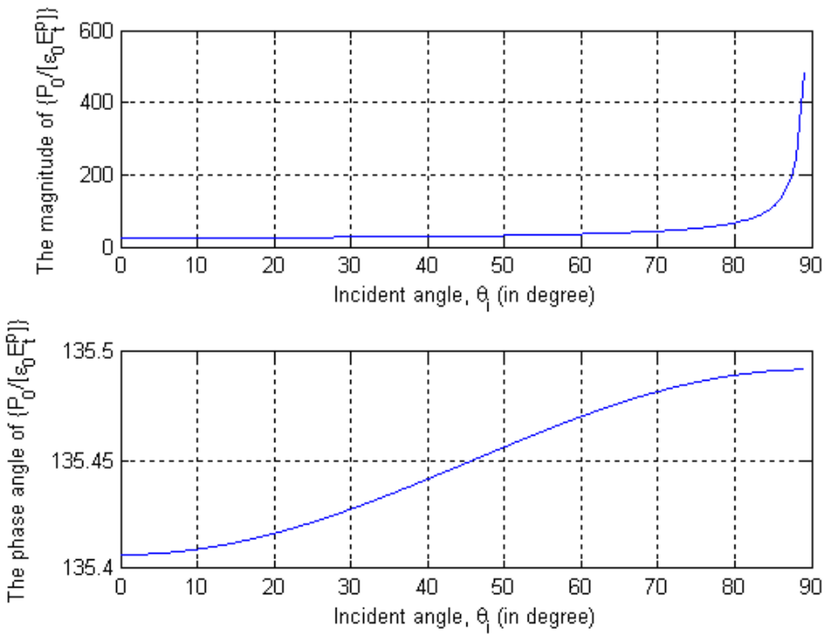

Fig. 8. The permanent defect polarization (at $\theta_0 = 0^\circ$) with respect to the incident angle of a red light of 1.98 eV (most significant when $\theta_i = 90^\circ$.)

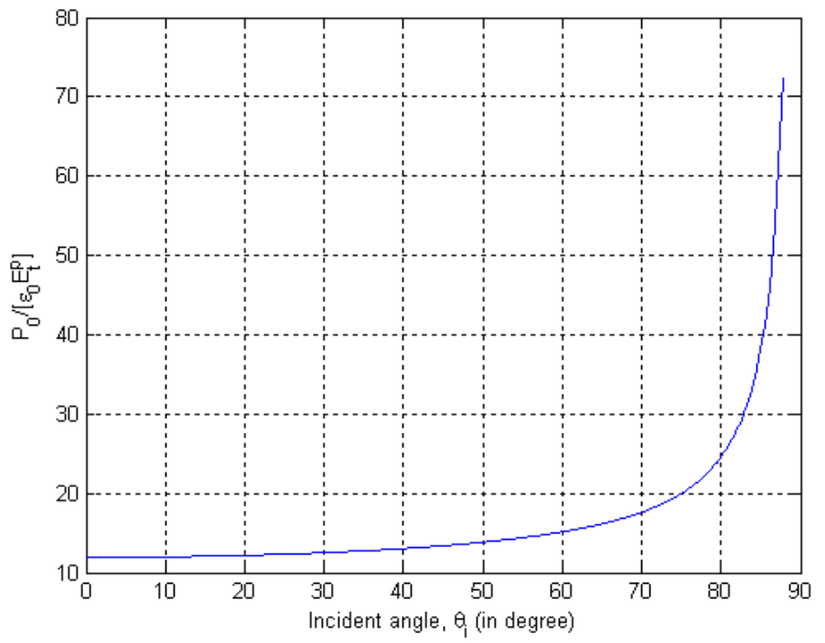

Fig. 9. The permanent defect polarization (at $\theta_0 = 0^\circ$) with respect to the incident angle of an infrared light of 0.83 eV energy (most significant when $\theta_i = 90^\circ$.)

Using the aforementioned calculation procedure, a considerable shift of the original Brewster angle of 77.2° to the new one of 72.5°, due to the vacancy defects replacement, is evident in Fig. 10 for the red light case. Note that the reflection for red light decreased

somewhat post the dipole engineering treatment. For the second IR case, Fig. 9 shows the involved action of the permanent defect polarization. A noticeable shift of the Brewster angle from 74.9° to 78.7° results (see Fig. 11). Moreover, this new Si material manifests higher reflection (or, *opaqueness*) (see Fig. 11), in addition to relatively high dissipation (see Fig. 7) for the IR light, after the proposed treatment.

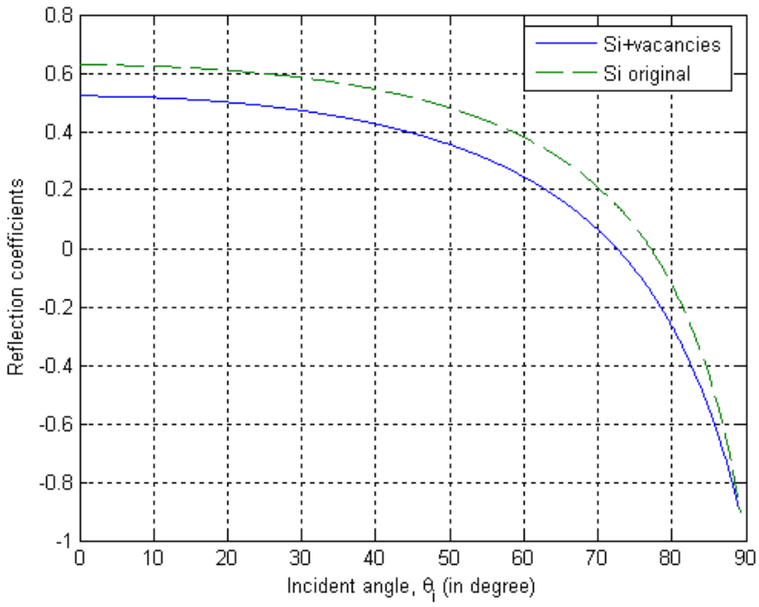

Fig. 10. Shift of the original Brewster angle (77.21°) to the new one (72.52°) for an incident light of energy 1.98 eV by the proposed vacancy defects introduction.

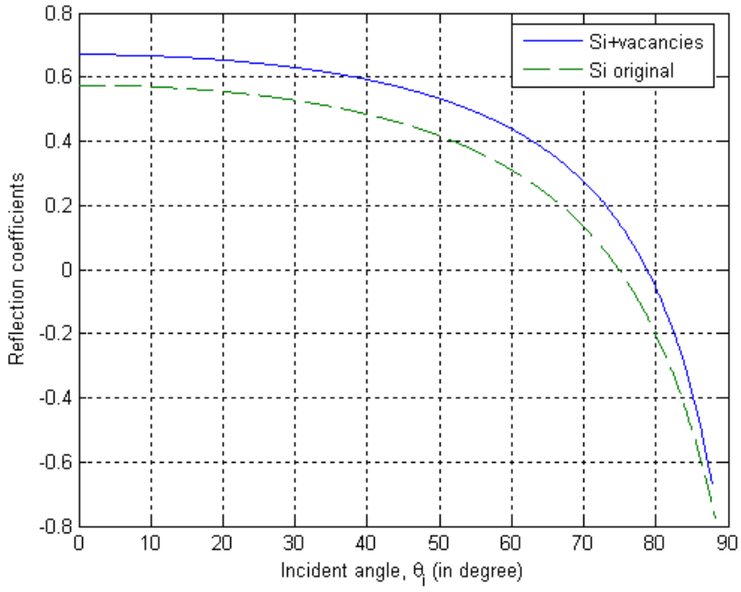

Fig. 11. Shift of the original Brewster angle (74.9°) to the new one (78.7°) for an incident light of energy 0.83 eV by the proposed vacancy defects introduction.

In the above, the shifted Brewster angles for both cases are associated with considerable dissipation caused by the introduced defects, as implied by Fig. 7. In particular, the defect-modified silicon wafer would absorb the total power of the p-wave incident at the Brewster angle. Nonetheless, this should not represent as sure characteristics for the general situations. For example, a θ_B-altering surface material (to be coated on the original host in a post-process manner) may have its permanent polarization implemented via replacing some of its atoms with other elements, instead of vacancies, and thus may not show such dissipating behavior.

6. Poled PVDF films and asymmetric reflection experiments

6.1 Background on the PVDF material ((Pallathadka, 2006), (Zhang et al., 2002)) and its preparations

Polyvinylidene difluoride, or PVDF (molecular formula: $-(CH_2CF_2)_n-$), is a highly non-reactive, pure thermoplastic and low-melting-point (170°C) fluoropolymer. As a specialty plastic material in the fluoropolymer family, it is used generally in applications requiring the highest purity, strength, and resistance to solvents, acids, and bases. With a glass transition temperature (T_g) of about -35°C, it is typically 50-60% crystalline at room temperature. However, when stretched into thin film, it is known to manifest a large piezoelectric coefficient of about 6-7 pCN^{-1}, about 10 times larger than those of most other polymers. To enable the material with piezoelectric properties, it is mechanically stretched and then poled with externally applied electric field so as to align the majority of molecular chains ((Pallathadka, 2006) , (Zhang et al., 2002)). These polarized PVDFs fall in 3 categories in general, i.e., alpha (TGTG'), beta (TTTT), and gamma (TTTGTTTG') phases, differentiated by how the chain conformations, of trans (T) and gauche (G), are grouped. FTIR (Fourier transform IR) measurements are normally employed for such differentiation purposes ((Pallathadka, 2006) , (Zhang et al., 2002)). With variable electric dipole contents (or, polarization densities) these PVDF films become ferroelectric polymers, exhibiting efficient piezoelectric and pyroelectric properties, making them versatile materials for sensor and battery applications.

In our experiments, PVDF films of Polysciences (of PA, USA) are subjected to non-uniform mechanical and electric polings to generate β-PVDF films of distributed dipolar regions. By applying infrared light beams on these poled β-PVDF films, the evidences of enhanced asymmetric refraction at varying incident angles as well as its inverse dependence on the incident power are sought for.

6.2 FTIR measurement setup

The adopted experimental setup takes full advantage of the original commercial FTIR measurement structure (Varian 2000 FT-IR) (Chen et al., 2008). The intended investigations are facilitated by putting an extra polarizer (Perkin-Elmer) in front of the detector and some predetermined number of optical attenuators (Varian) before the sample (see, Fig. 12). Figs. 13(a) and 13(b) show the detector calibration results under different numbers of attenuating sheets for both the p- and s-wave incidence, respectively. As is obvious, the detected intensities degraded linearly with the number of attenuators installed and the spectra remain morphologically similar.

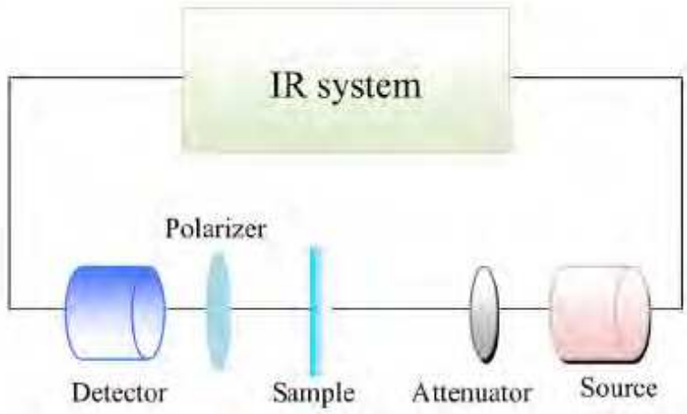

Fig. 12. FTIR measurement setup.

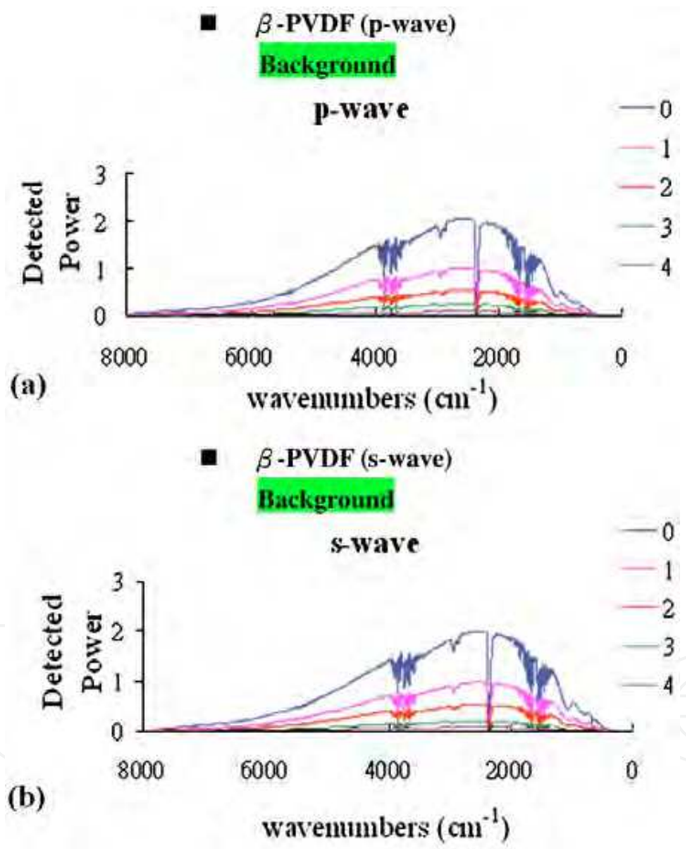

Fig. 13. Calibration on detected spectral effects when employing different numbers of attenuators under normal incidence of (a) p- and (b) s-polarized lights, respectively.

6.3 Evidence of asymmetric reflections and enhanced reflectivities for attenuated incident lights

In the reflectivity ($R \equiv r^2 = |E_{r0}/E_{i0}|^2$) experiments, each electrically-poled β-PVDF film (thickness 16-18 μm) is subjected to IR light irradiation at varying incident angles and beam

intensities (via using the above attenuator films) (Chen et al., 2008). Even though a PVDF film encompasses many double layers along its thickness, the reason the above theoretical derivations based on a single double layer (see Fig. 5) should still apply is that there are non-uniform vertical polarizations (or, electric fields) at the surface. In other words, the resultant gradients in the incident-light-responsive planar dipole moment would then render nonzero interfacial jump of $E_{||}$ as addressed by Eq. (26).

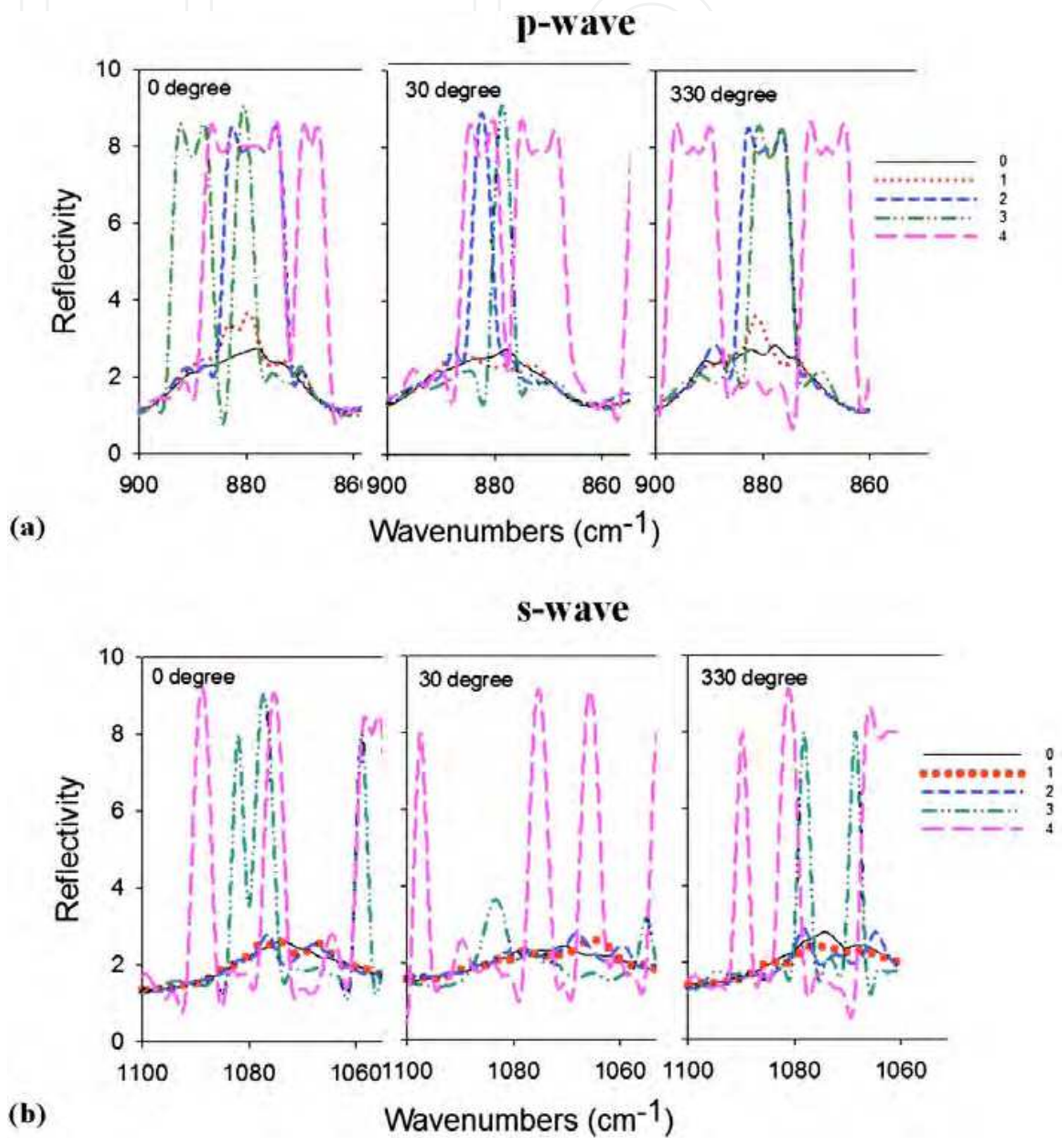

Fig. 14. Experimental results on asymmetric reflection among conjugate light paths and enhanced reflectivity at different numbers of attenuators.

Since it is the reflectivity that is of interest, at each incident angle and under a specified degree of attenuation, the reflection is normalized with respect to the corresponding reference value in the absence of a PVDF film as shown in Fig. 13 (a) and 13 (b) (Chen et al., 2008). Figs. 14 (a) and 14 (b) illustrate the arising of asymmetric reflections between

conjugate incident paths (e.g., incidence at 30° versus 330°) for both the p- and s-polarized infrared lights under various degrees of intended attenuation (Chen et al., 2008). In the above, the incident angle is defined by rotating clockwise the poled-PVDF sample under top-view of the setup of Fig. 12. Hence, reversing the light reflection path indeed causes a different reflected power to arise, as predicted by the aforementioned theoretical exploration. Note that, however, in traditional FTIR measurements, decrease in the detected intensity has been routinely attributed to increased absorption by PVDF films. Nevertheless, for an obliquely incident light the beam path within PVDF is only slightly larger than that in a normal incident situation. Thus, the resultant infinitesimal increase in PVDF absorption should never be sufficient to account for the detected large difference in reflected power. Notably, the detected decrease in intensity should instead be attributed to enhanced reflection caused by distributed dipoles on the poled PVDF films.

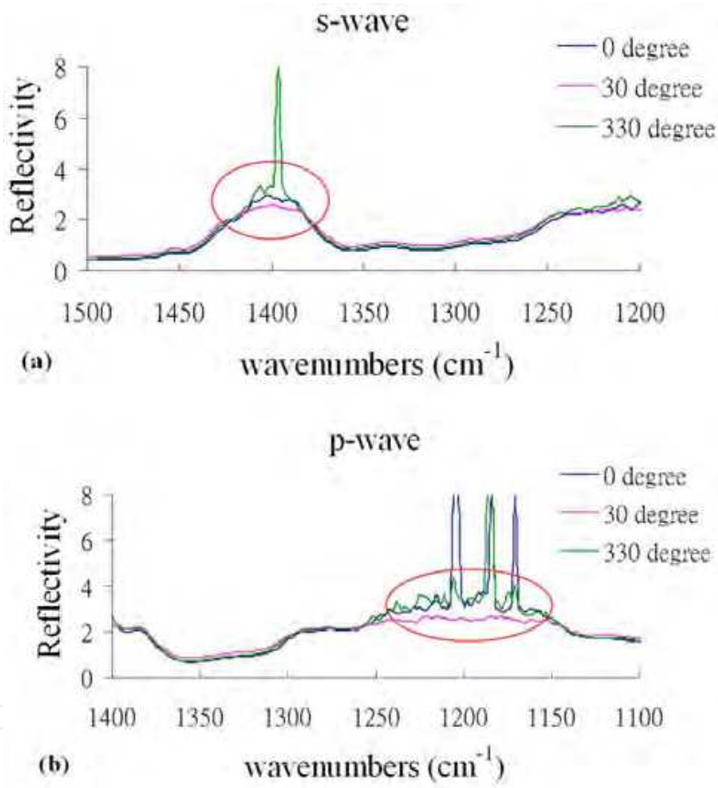

Fig. 15. Observed distinct asymmetric reflection among conjugate light paths under two attenuator films and at varying incident angles.

Furthermore, for both p- and s-polarized incident waves, the variations in reflectivity are more significant in the situations where more attenuation is imposed, complying with the above theoretical expectation. Namely, the second terms in the above-derived Eqs. (28) and (29) are more enhanced under the situation of smaller incident light electric field (or power). Lastly, even though the appearance of FTIR-detected spiky saturation peaks in Figs. 14 (a) and 14 (b) actually imply loss in the signal-to-noise ratios when under heavy attenuation of the incident power, several unsaturated features, e.g., in Figs. 15(a) and 15(b) still remain (wherein 2 sheets of attenuators are employed) (Chen et al., 2008). Such evidenced spectral

features strongly endorse the above theoretical claim that the reflectivity variation of a dimmer light is more outstanding than that of a brighter one.

7. PVDF experiment on varying Brewster angle

7.1 PVDF new Brewster angle

The experimental set up is as arranged in Fig. 16, where a light beam of 0.686 mm radius from the He-Ne laser (of the wavelength of 632.8 nm) is converted into p-wave mode after getting through the polarizer (Tsai et al., 2011). Two double convex lenses, with focal lengths being 12.5 cm and 7.5 cm, respectively, are for shrinking down the beam radius to 0.19 mm to reduce the width of light reflection off the PVDF surface. The reflected light is then further focused by a lens (of 2.54 cm focal length) before reaching the diode power detector. An incident angle range is scanned from 50.5°to 59.5°(θ_i) with an accuracy of 0.015°, and then its conjugate range from -50.5°to -59.5°($-\theta_i$), while the incident light intensity is varied between 100% (8.54 mW) and 10% power by moving an attenuator into or withdrawing from the beam path.

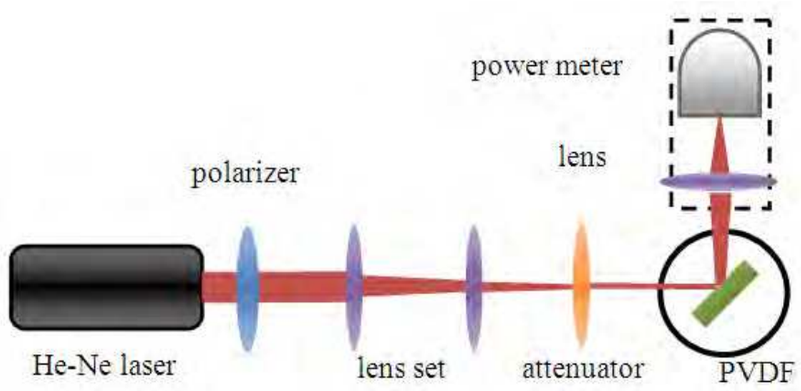

Fig. 16. Configuration of PVDF Brewster angle measurement.

The fitted curves for the measured Brewster angles for the two conjugate incident paths, under 100% and 10% laser beam intensities, on both the β- and poled-β films, are shown in Fig. 17 and Fig. 18, respectively (Tsai et al., 2011). It can be seen that Brewster angles measured via the two conjugate incident paths differ considerably. Such difference becomes more outstanding on the poled-β PVDF film, and in particular, when the laser beam is attenuated to 10%, as predicted by the theory of the authors (Liao et al., 2006). The typical data are given in Table 1.

Parameters	Beam intensity	$\theta_B(\theta_i)$	$\theta_B(-\theta_i)$	$\Delta\theta_B$
β-PVDF	100 %	54.7925°	55.1475°	0.355°
	10 %	54.695°	55.3875°	0.6925°
Poled-β PVDF	100 %	54.62°	55.77°	1.05°
	10 %	54.38°	56.245°	1.865°

Table 1. PVDF Brewster angles measurement.

It is noted that although even the intrinsic α phase PVDF possesses birefringence and this can lead to different Brewster angles as in the above too, the difference degree is at most around 0.129°, and hence may be ignored.

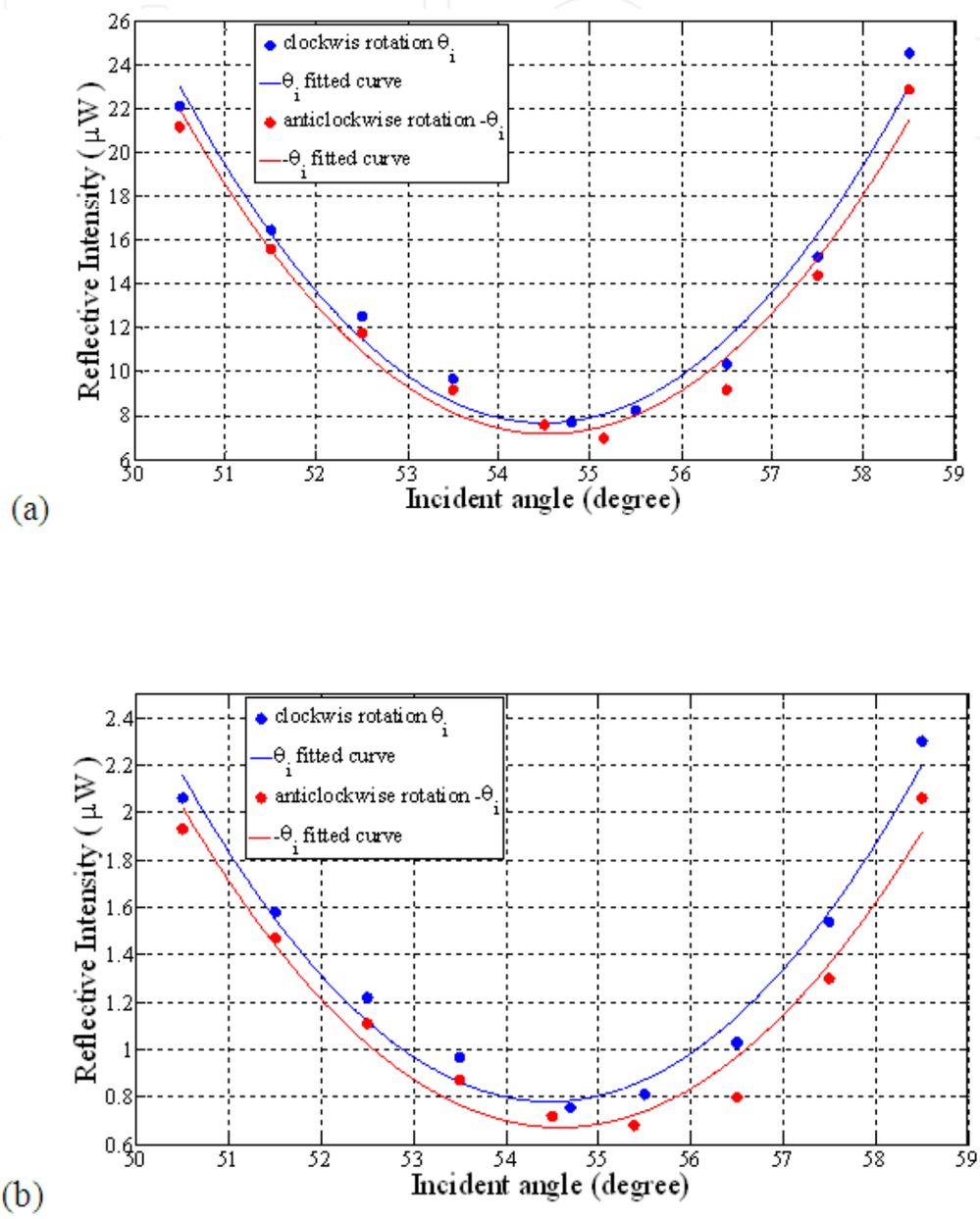

Fig. 17. Measured Brewster angles on • β-PVDF for two conjugate incident paths, under: (a) 100% laser intensity, (b) 10% laser intensity (only one-tenth of data points are shown)

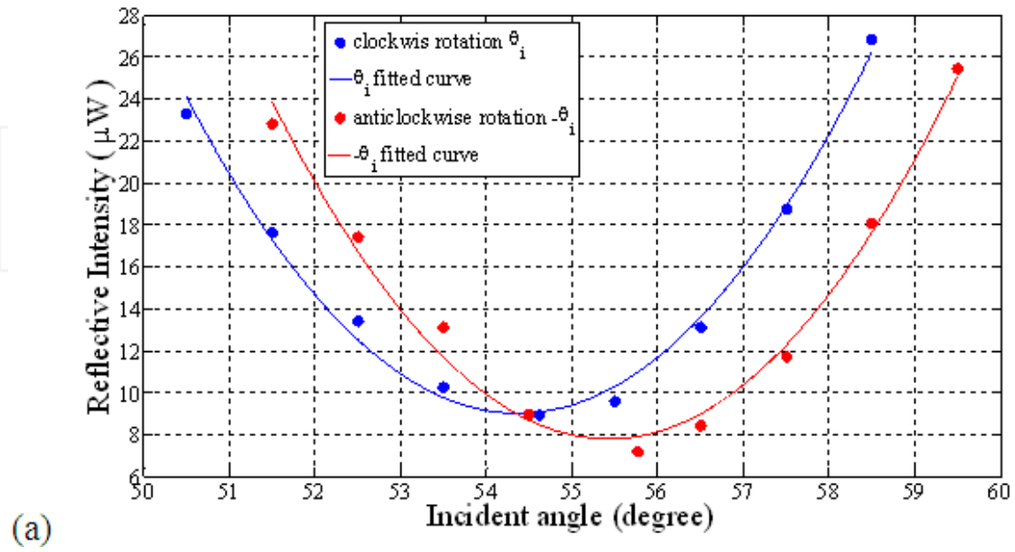

(a)

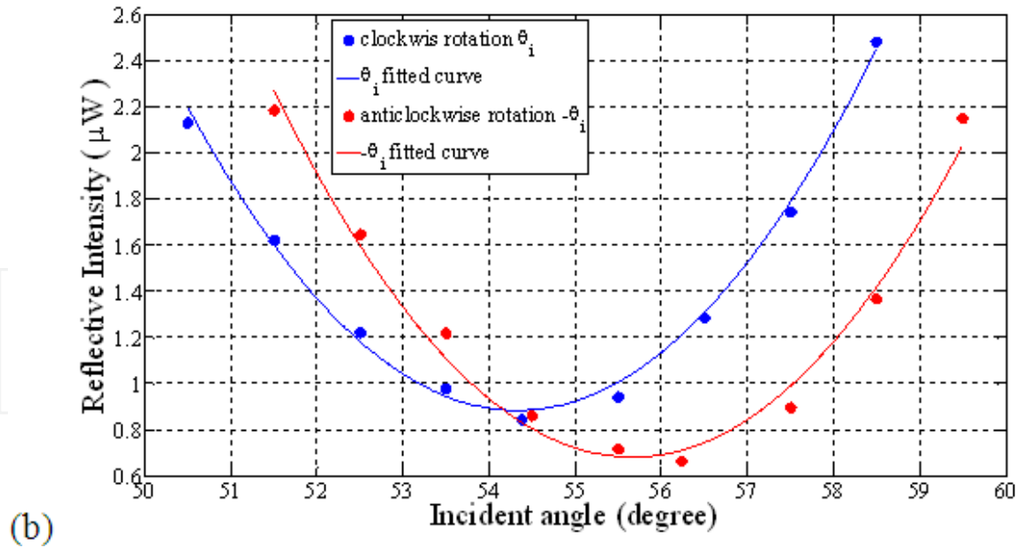

(b)

Fig. 18. Measured Brewster angles on poled ・β-PVDF for two conjugate incident paths, under: (a) 100% laser intensity, (b) 10% laser intensity (only one-tenth of data points are shown)

This can be verified by putting into Eq. (23) the known ordinary and extraordinary refractive indices of PVDF and getting the Brewster angles of 54.814° and 54.933°, respectively. Further, the fact that the larger deviation is evidenced in the poled-β phase, as compared with that from the β phase, indicates that permanent dipoles are indeed the cause of such alteration in Brewster angles.

By putting the above experimental data (i.e., Table 1) into Eq. (23), the relative dielectric coefficients ($\tilde{\varepsilon}_r$) for both the β- and poled-β PVDF films are extracted and tabulated in Table 2 (Tsai et al., 2011).

Parameters	Beam intensity	$\tilde{\varepsilon}_r(\theta_i)$	$\tilde{\varepsilon}_r(-\theta_i)$
β-PVDF	100 %	2.008	1.994
	10 %	2.062	2.1
Poled-β PVDF	100 %	1.983	1.948
	10 %	2.16	2.239

Table 2. Relative dielectric coefficients through fitting experimental data.

Then, the averaged effective permanent polarization $P_0(\omega)$ and orientation θ_0 can be extracted through trial-and-error (see, Table 3) by putting these coefficients into Eqs. (22) and (24), and using the relations: $E_t^p = t_p \cdot E_i^p$ and $t^p = 2n_{air}\cos\theta_i / \left(n_{air}\cos\theta_t + n_t\cos\theta_i\right)$. In the above, $E_i^p = \sqrt{S/\varepsilon_0 C}$, $\theta_t = \sin^{-1}\left(n_{air}/n_t \sin\theta_i\right)$, with S, ε_0, and C being the irradiating light intensity per unit area, the vacuum permittivity (i.e., $8.85 \cdot 10^{-12}$ F/m), and the light speed in vacuum, respectively, and $\varepsilon_r = n_o^2$ (Tsai et al., 2011).

Parameters	θ_0	$P_0(\omega)$
β-PVDF	41.64°	$1.0226 \times 10^{-9}\left(C/m^2\right)$
Poled-β PVDF	61.62°	$1.7843 \times \times 10^{-9}\left(C/m^2\right)$

Table 3. Extracted effective permanent polarizations and orientations of dipole-engineered PVDF films.

It can be seen that the electro-poling has caused the permanent polarization to increase somewhat, and most of all, its orientation with respect to the interface to add around 20°.

7.2 Novel 2D refractive index ellipse

Owing to its intrinsic uniaxial birefringence property ((Matsukawa et al., 2006), (Yassien et al., 2010)), when a light is incident upon a PVDF film (as formed, without poling), the

refracted light is decomposed into an ordinary wave and an extraordinary wave, which correspond to refractive indices of n_o and n_e, respectively. Namely, when the plane-of-incident is formed by the light's propagating direction vector $\bar{k}$ and the uniaxis $\hat{z}$ (see, Fig. 19), with the angle between them being θ, then a slice on the 3D refractive index ellipsoid cutting perpendicular to $\bar{k}$ will give rise to an elliptic contour which is of the minor axis n_o and major axis n_s in a relationship expressed as:

$$\frac{1}{n_s^2(\theta)} = \frac{cos^2\theta}{n_o^2} + \frac{sin^2\theta}{n_e^2} \tag{30}$$

However, the whole picture will change considerably in the presence of ordered permanent dipoles. Namely, unlike the traditional elliptic contour in red color in the polar diagram Fig. 20, unconventional contours in blue and green represent 2D (two dimension) refractive index surfaces of the situation on β-PVDF (i.e., $\theta_0 = 41.64°$) under 100 % and 10 % laser power, respectively; and those in purple and orange colors are on poled-β PVDF (i.e., $\theta_0 = 61.62°$) under 100 % and 10 % laser power, respectively (Tsai et al., 2011). Note that, in Fig. 20, as the ordinate dimension is along the direction of interface (in green) and the abscissa along the norm in real setup, both the I and III quadrants describe the refraction in the incident angle range of 0°~ 90° (i.e., θ_i), and quadrants II and IV depicts that of 0°~ -90° (i.e., $-\theta_i$). Hence, the dipole-engineered ones would demonstrate open splittings near the traditional incident angles. Among them, the deviation should be more outstanding for the case with the test film being poled-β than β-PVDF, and especially when at lower incident laser power (Tsai et al., 2011).

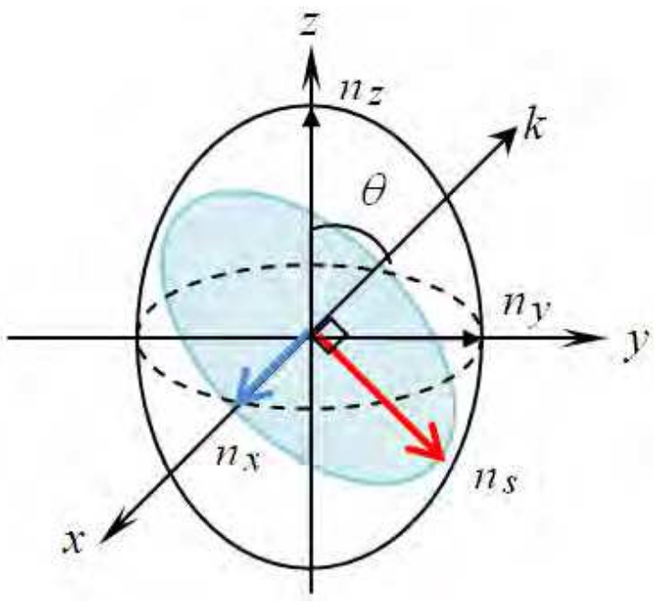

Fig. 19. Construction of the refractive index surface.

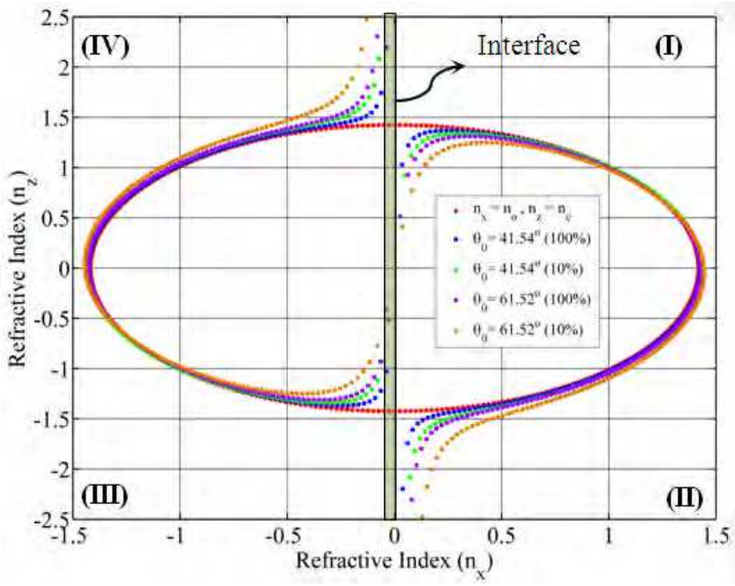

Fig. 20. The polar diagram for refractive index distribution.

Experimentally, the following tendency was observed when the test samples were altered from normal to β- and then to poled-β PVDF films. When the incident angles was within the I- and III- quadrants (i.e., θ_i), the evidenced Brewster angles shrunk and the refractive index became smaller (i.e., $\tilde{\varepsilon}_r < \varepsilon_r$). On the other hand, when the laser was incident in the II- and IV- quadrants (i.e., $-\theta_i$), both the Brewster angles and the refractive index ($\tilde{\varepsilon}_r > \varepsilon_r$) switched to larger values. This tendency apparently goes with the above theoretical prediction.

7.3 Notable indication on traditional SPR measurements

Facilitated by its very high-Q resonance angle, the surface plasmon resonance (SPR) type of techniques, and their variations, are known to be very sensitive tools for measurements of refractive indices ($n = \sqrt{\varepsilon_r \mu_r}$). Among them, the one using prism coupling and in the so-called "Kretschmann-Raether (KR) configuration" ((Maier, 2007), (Raether, 1988)), is probably the most widely adopted practice. That is, the KR- configured materials from top down is arranged to be: prism (the "0" matter), metal film (the "1" matter), air gap, target under test (the "2" matter), and buffer layer (the "3" matter). When a p-wave is incident at a so-called "resonance angle" onto the topmost KR-configured plane (i.e., at "0"-"1" interface), a surface resonant plasma wave is excited at the metal-air interface, leading to a minimum in light reflection ((Maier, 2007), (Raether, 1988)).

The overall reflection coefficient (of an incident p-wave) off this 4-material KR configuration can be derived from using the Fabry-Perot interference principle and is ((Maier, 2007), (Raether, 1988)):

$$r_{0123}^{p} = \frac{r_{01}^{p} + \dfrac{r_{12}^{p} + r_{23}^{p} e^{i2\phi_2}}{1 + r_{12}^{p} r_{23}^{p} e^{i2\phi_2}} e^{i2\phi_1}}{1 + r_{01}^{p} \dfrac{r_{12}^{p} + r_{23}^{p} e^{i2\phi_2}}{1 + r_{12}^{p} r_{23}^{p} e^{i2\phi_2}} e^{i2\phi_1}} \tag{31}$$

And, the overall reflectivity in power is: $R = \left| r^{p}_{0123} \right|^2$, where r^{p}_{01}, r^{p}_{12}, r^{p}_{23} are reflection coefficients at "0"-"1", "1"-"2", and "2"-"3" interfaces according to the traditional Fresnel equations; and $\phi_i = k_0 \sqrt{\varepsilon_i} cos\theta_i d_i$ are phase angles associated with matters "1" and "2", respectively; and k_0 is incident wave vector; and ε_1 / d_1 and ε_2 / d_2 are relative dielectric coefficient / layer thickness of the metal film and material under test, respectively.

However, it is found in the above experiments that in the presence of permanent dipoles, not only is the Brewster angle dependent on the incident light power as well as the dipole orientation, but also that two conjugate incident light paths result in distinctively different refractions. Therefore, although the form of Eq. (31) remains the same in the presence of permanent dipoles, values of local reflection coefficients involved can vary considerably from those of their classical counterparts. In other words, the traditional confidence in SPR type of measurements may be in jeopardy when the material under test is embedded with permanent dipoles, as will be shown in what follows.

Consider a KR-configured SPR measurement setup as an example. It includes: a lens (SF 11) of relative dielectric coefficient of $(1.7786)^2$, a silver metal film of 52 nm (d_1) thickness of a relative dielectric coefficient of $-17.6 + 0.67i$ (Raether, 1988), a PVDF film (as grown, or β, or poled-β) as the material under test of thickness of about 15 μm (d_2), with its original relative dielectric coefficients being n_o^2 and n_e^2, and a buffer layer of air of a relative dielectric coefficient of about 1. This configuration is then subjected to the irradiation of a light beam , from a 632.8 nm wavelength He-Ne laser, of the incident angles ranging within 50°~70°(θ_i) and its conjugate counterpart paths within the angle range -50°~ -70°($-\theta_i$).

The numerical calculation result based on the above setup is shown in Fig. 21 and indicates the following (Tsai et al., 2011). The birefringence (i.e., n_e besides n_o) of as-grown PVDF suffices to give a maximal SPR resonance angle deviation of about 0.5° (away from 58°). This deviation of resonance angles is considerably amplified in the β-(2.5°) and poled-β (4°) cases, owing to the increase of permanent polarization density and alignment. In such sensitive SPR type of measurements, these large deviations of resonance angles represent large distortions in the light reflectivity, as illustrated in Fig. 21. Notably, it also affirms the theoretical prediction (see, Eq. (24)) that the reflectivity coefficient is inversely proportional to the strength of the incident (or, transmitted) light electric field. All these findings indicate that traditional SPR type of measurements needs to exercise precaution when the material under test is embedded with permanent dipoles. For example, most living cells are with cell walls made of two opposite double layers of dipolar molecules (Alberts et al., 2007).

8. The quasistatic macroscopic mixing theory for magnetic permeability

Although mixing formulas for the effective-medium type of approximations for the dielectric permittivities in the infinite-wavelength (i.e., quasistatic) limit (Lamb et al., 1980), such as the Maxwell Garnett formula (Garnett, 1904), have been popularly applied in the whole spectral range of electromagnetic fields, their magnetic counterpart has seldom been addressed up to this day. The current effort is thus to derive such an equation to approximately predict the final permeability as the result of mixing together several magnetic materials (Chang & Liao, 2011).

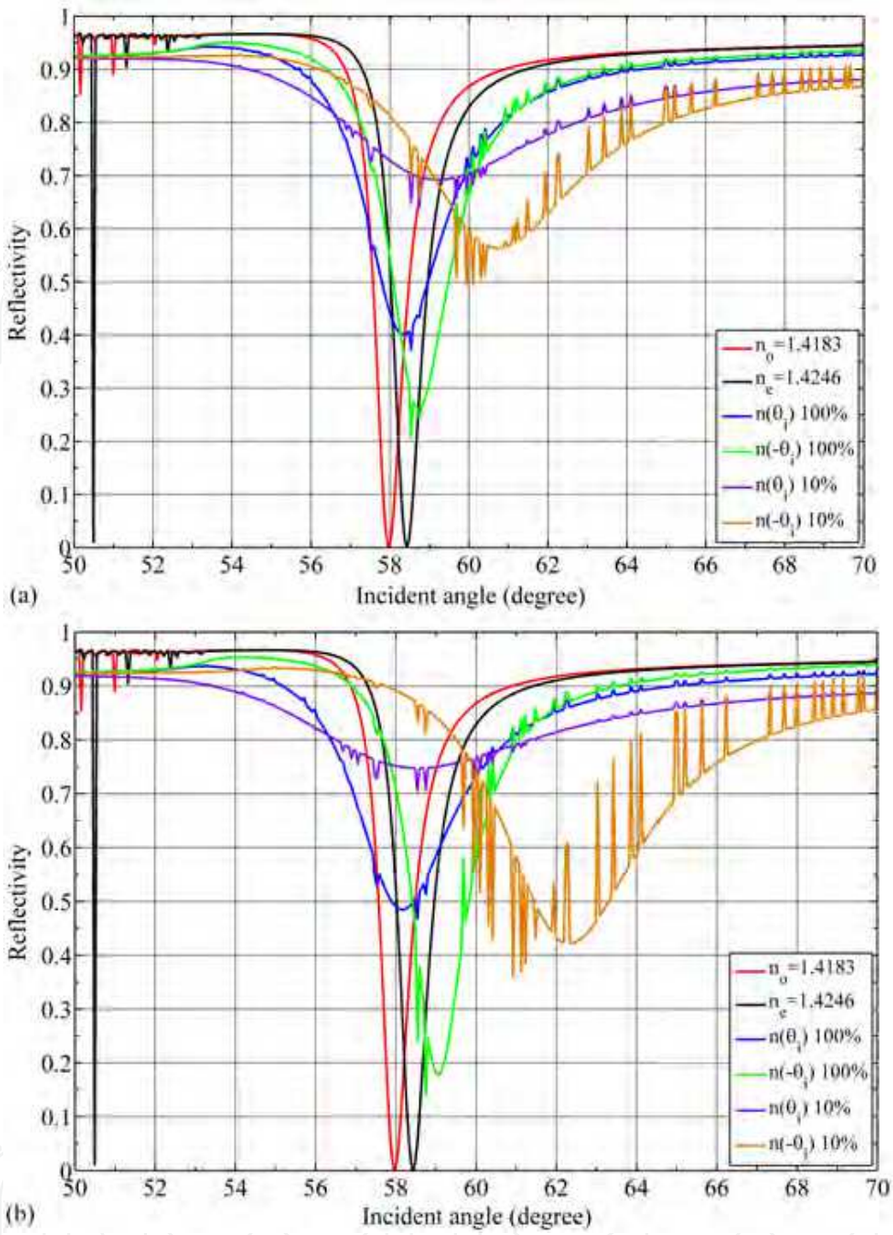

Fig. 21. Calculated SPR reflectivities for: (a) β-PVDF, (b) poled-β-PVDF.

8.1 A brief review of the derivation leading to the Maxwell Garnett and Bruggeman formulas

Historically, an isotropic host material was hypothesized to embed with a collection of spherical homogeneous inclusions. With the molecular polarization of a single molecule of such inclusions being denoted *a*, the following relation was established within the linear range (Cheng, 1989):

$$\vec{p}_m = \alpha \varepsilon_0 \vec{E}_m \tag{32}$$

where $\vec{p}_m$ was the induced dipole moment and $\vec{E}_m$ was the polarizing electric field intensity at the location of the molecule. Since the treatment was aiming for uniform spherical inclusions, the polarizability became a scalar, such that $\vec{E}_m$ was expressed as (Purcell, 1985):

$$\vec{E}_m = \vec{E} + \vec{E}_p + \vec{E}_{near} \tag{33}$$

Here $\vec{E}$ was the average field within the bulk host, $\vec{E}_p$ was the electric field at this molecular location caused by all surrounding concentric spherical shells of the bulk, and $\vec{E}_{near}$ was due to asymmetry within the inclusion. In those cases of interest where either the structure of the inclusion was regular enough, such as a cubical or spherical particulate, or all incorporated molecules were randomly distributed, $\vec{E}_{near}$ became essentially zero. It was further approximated that $\vec{E}_m = \vec{E} + \vec{P}/(3\varepsilon_0)$ (Purcell, 1985), to be elaborated later, with $\vec{P}$ being the polarization density associated with a uniformly polarized sphere, and ε_0 being the permittivity in free space. Hence, given Eq. (32), with the number density of such included molecules denoted as n, and $\vec{P} = n\vec{p}_m$ (Cheng, 1989), the polarization density was further expressed as:

$$\vec{P} = n\alpha\varepsilon_0\left[\vec{E} + \vec{P}/(3\varepsilon_0)\right] \tag{34}$$

However, it was well-known that for isotropic media $\vec{P} = (\varepsilon_r - 1)\varepsilon_0\vec{E}$ where ε_r stood for the relative permittivity (i.e., the electric field at the center of a uniformly polarized sphere (with $\vec{P}$ being its polarization density) was $-\vec{P}/(3\varepsilon_0)$). Then, a relation known as the Lorentz-Lorenz formula readily followed ((Lorenz, 1880), (Lorentz, 1880)):

$$\alpha = \frac{3(\varepsilon_r - 1)}{n(\varepsilon_r + 2)} \tag{35}$$

In those special cases where the permittivity of each tiny included particle was ε_s and the host material was vacuum (ε_r =1), such that $n = V^{-1}$ (V being the volume of the spherical inclusions), and Eq. (35) would have to satisfy (Garnett, 1904):

$$\alpha = 3V\frac{\varepsilon_s - \varepsilon_0}{\varepsilon_s + 2\varepsilon_0} \tag{36}$$

Combining Eqs. (35) and (36) gave the effective permittivity (ε_{eff}) of the final mixture (Garnett, 1904):

$$\varepsilon_{eff} = \varepsilon_r\varepsilon_0 = \varepsilon_0 + 3f\varepsilon_0\frac{\varepsilon_s - \varepsilon_0}{\varepsilon_s + 2\varepsilon_0 - f(\varepsilon_s - \varepsilon_0)} \tag{37}$$

with $f = nV$ being the volume ratio of the embedded tiny particles ($0 \le f \le 1$) within the final mixture. If, instead of vacuum, the host material was with a permittivity of ε_h, Eq. (37) was then generalized to the famous Maxwell Garnett mixing formula:

$$\varepsilon_{eff} = \varepsilon_h + 3f\varepsilon_h\frac{\varepsilon_s - \varepsilon_h}{\varepsilon_s + 2\varepsilon_h - f(\varepsilon_s - \varepsilon_h)} \tag{38}$$

For the view in which the inclusion was no longer treated as a perturbation to the original host material, Bruggeman managed to come up with a more elegant form wherein different ingredients were assumed to be embedded within a host (Bruggeman, 1935). By utilizing Eqs. (35) and (36), he had:

$$\frac{\varepsilon_{eff}-\varepsilon_0}{\varepsilon_{eff}+2\varepsilon_0}=\sum_i f_i\frac{\varepsilon_i-\varepsilon_0}{\varepsilon_i+2\varepsilon_0} \tag{39}$$

where f_i and ε_i are the volume ratio and permittivity of the i-th ingredient.

8.2 The magnetic flux density at the center of a uniformly magnetized sphere

surface current can be expected to appear on the surface of a uniformly magnetized sphere (wherein $\vec{M}$ is the finalized net anti-responsive magnetization vector, see Fig. 22).

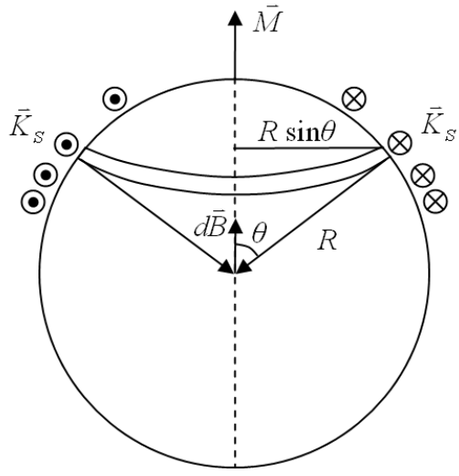

Fig. 22. Situation for calculation of the central magnetic flux density on a uniformly magnetized sphere.

In Fig. 22, $\vec{K}_S$ is the induced anti-reactive surface current density (in A/m) on the sphere's surface. By integrating all surface current density on strips of the sphere's surface the magnetic flux density ($\vec{B}_c$) at the center of a uniformly magnetized sphere is obtained to be (Lorrain & Corson, 1970):

$$\vec{B}_c=\frac{2\vec{M}\mu_0}{3} \tag{40}$$

8.3 Magnetic permeabilities formula mixing

Now, this time consider an isotropic host material embedded with a collection of spherical homogeneous magnetic particles. Given the magnetic flux density at the location of a single molecule of the inclusions being $\vec{B}_m$, the following relation holds in general:

$$\vec{B}_m = \vec{B} - \vec{B}_c + \vec{B}_{near} \tag{41}$$

where $\vec{B}$ is the average magnetic flux density within the bulk host and $\vec{B}_{near}$ is due to the asymmetry in the inclusion. In those cases of interest where either the structure of the included particles is regular enough, such as a cubical or spherical particulate, or all incorporated molecules are randomly distributed, $\vec{B}_{near}$ can be taken as zero.

If the magnetic field intensity at the location of the molecule is denoted $\vec{H}_m$, the induced magnetic dipole moment (m_m) is:

$$\vec{m}_m = \kappa_m \vec{H}_m \tag{42}$$

where κ_m is the molecular magnetization of the molecule. Because $\vec{M}$ equals $n\vec{m}_m$, we have (Cheng, 1989)

$$\vec{M} = n\kappa_m \vec{H}_m = \chi_m \vec{H}_m \tag{43}$$

where χ_m is known as the magnetic susceptibility. Hence, $\vec{B}_m$ can be further expressed as (Cheng, 1989)

$$\vec{B}_m = \mu_0 \mu_r \vec{H}_m = \mu_0 \left(1 + n\kappa_m\right) \vec{H}_m = \mu_0 \left(1 + \chi_m\right) \vec{H}_m \tag{44}$$

with μ_r being the relative permeability. By incorporating Eq. (41) and Eq. (44) into Eq. (43) we obtain:

$$M = \frac{n\kappa_m}{\mu_0 \left(1 + n\kappa_m\right)} \left(B - \frac{2M\mu_0}{3} \right) \tag{45}$$

Further, for isotropic magnetized materials (Cheng, 1989):

$$M = \left(\mu_r - 1\right) H = \frac{\left(\mu_r - 1\right) B}{\mu_0 \mu_r}, \text{ or}$$

$$B = \frac{\mu_0 \mu_r}{\left(\mu_r - 1\right)} M \tag{46}$$

Substituting Eq. (46) into Eq. (45) gives (Chang & Liao, 2011)

$$\kappa_m = \frac{3}{n} \left(\frac{\mu_r - 1}{-2\mu_r + 5} \right) \tag{47}$$

In the special case where the host material is vacuum (μ_r = 1) and the permeability of the spherical particles is μ_s, $n = V^{-1}$ (V being the volume of a spherical particle), and Eq. (47) is satisfied by:

$$\kappa_m = 3V \frac{\mu_s - \mu_0}{-2\mu_s + 5\mu_0} \tag{48}$$

Combining Eqs. (47) and (48) gives the effective permeability (μ_{eff}) of the final mixture, i.e. (Chang & Liao, 2011),

$$\mu_{eff} = \mu_r \mu_0 = \mu_0 + 3 f \mu_0 \frac{\mu - \mu_0}{-2\mu + 5\mu_0 + 2 f \left(\mu - \mu_0\right)} \tag{49}$$

Where $f = nV$ is the volume ratio of the embedded particles within the mixture ($0 \le f \le 1$). In the more general situations where the host is no longer vacuum but of the permeability μ_h, then the more general mixing formula of permeabilities becomes (Chang & Liao, 2011):

$$\mu_{eff} = \mu_h + 3 f \mu_h \frac{\mu_s - \mu_h}{-2\mu_s + 5\mu_h + 2 f \left(\mu_s - \mu_h\right)} \tag{50}$$

As with Bruggeman's approach for dielectrics (Bruggeman, 1935), the derived magnetic permeability formula can be generalized to the multi-component form (Chang & Liao, 2011):

$$\frac{\mu_{eff} - \mu_0}{-2\mu_{eff} + 5\mu_0} = \sum_i f_i \frac{\mu_i - \mu_0}{-2\mu_i + 5\mu_0} \tag{51}$$

where f_i and μ_i denote the volume ratios and permeabilities of the involved different inclusions, respectively. Or (Chang & Liao, 2011),

$$\frac{\mu_{reff} - 1}{-2\mu_{reff} + 5} = \sum_i f_i \frac{\mu_{ri} - 1}{-2\mu_{ri} + 5} \tag{52}$$

Although the actual mixing procedures can vary widely such that substantial deviations may result between the theoretical and measured values, Eq. (52) should still serve as a valuable guide when designing magnetic materials or composites.

9. A practical method to secure magnetic permeability in optical regimes

As widely known, electronic polarization is involved in the absorption of electromagnetic wave within materials and this mechanism is represented by permittivity even in light-wave frequencies. However, refractive index which describes light absorption and reflection is calculated in terms of permittivity and permeability (accounting for magnetization). But permeability spectra in light frequencies are hardly available for most materials. In contrast with it, permeabilities for various materials are fairly well documented at microwave frequencies (see, for example, (Goldman, 1999) and (Jorgensen, 1995)). It is noted that more often than not an electronic permittivity spectrum ($\varepsilon_r(\omega)$) is secured by measuring its corresponding refractive index ($N(\omega)$) while bluntly assuming its relative permeability (μ_r) to be unity. Obviously, this approach is one-sided and inappropriate. In particular, as we are entering the nanotech era, many new possibilities should emerge and surprise us with their novel optical permeabilities, for example, the originally nonmagnetic manganese crystal can be made ferromagnetic once its lattice constant is varied (Hummel, 1985). In this section, a method is proposed such that reliable optical permeability values can be obtained numerically.

The magnetic permeability of a specific material emerges fundamentally from wavefunctions of its electrons. In the popular density functional theory (DFT) approach, the

role of these electron wavefunctions is taken by the one-electron spinorbitals, called the Kohn-Sham orbitals ($|\psi_{os}\rangle$) (see, e.g., (Shankar, 1994) and (Atkins & Friedman, 1997)). A spinorbital is a product of an orbital wavefunction and a spin wavefunction:

$$|\psi_{os}\rangle = |\psi_{o}\rangle \otimes |\psi_{s}\rangle \tag{53}$$

where $|\psi_{o}\rangle$ is the orbital part, and $|\psi_{s}\rangle$ is the spin part of $|\psi_{os}\rangle$.

In the density functional theory, these spinorbitals are solutions to the equation:

$$\rho(\vec{r}) = \sum_{i=1}^{n} \left|\psi_{os_i}(\vec{r})\right|^2 , \tag{54}$$

where $\rho(\vec{r})$ is the local charge probability density function. Then, the exact ground-state electronic energy as well as other electronic properties of this *n*-electron system are known to be unique functions of ρ ((Shankar, 1994), (Atkins & Friedman, 1997)). Further, the overall wavefunction satisfying the Pauli exclusion principle is often expressed in terms of the Slater determinant ((Shankar, 1994), (Atkins & Friedman, 1997)) as:

$$\psi_{total}(\vec{r}) = (n!)^{-1/2} \det\left|\psi_{os_1}(\vec{r}) \cdot \psi_{os_2}(\vec{r}) \cdot \psi_{os_3}(\vec{r}) \cdots \psi_{os_n}(\vec{r})\right| , \tag{55}$$

Hence, the primitive transition rate of a typical electronic excitation within a material of interest can now be expressed in terms of the Fermi's golden rule ((Shankar, 1994), (Atkins & Friedman, 1997)) as:

$$R_{total} = C \cdot \sum_{f,i} \left|\left\langle \psi_{os}^{f0} \middle| H^1 \middle| \psi_{os}^{i0} \right\rangle\right|^2 \delta\left(E_{os}^{f0} - E_{os}^{i0} - \hbar\omega\right) , \tag{56}$$

where H^1 is the first order perturbation to the Hamiltonian of electrons caused by a light wave propagating within; ψ_{os}^{i0} (of E_{os}^{i0}) and ψ_{os}^{f0} (of E_{os}^{f0}) are the electron states (energies) before and after the perturbation (H^1) takes place, respectively; ω is the radian frequency of the propagating light wave; $\hbar$ is Planck constant divided by 2π; and *C* is a proportional constant. H^1 in Eq. (56) can be expressed as (Shankar, 1994):

$$H^1 = \frac{e}{2mc} \vec{A}_0 \cdot \vec{P}_M \tag{57}$$

where $\vec{A}_0$ is the vector potential of the injected light wave; $\vec{P}_M$ is the momentum operator of electrons in the material of interest. $\vec{P}_M$ represents electrons' straight-line motion which constitute electronic polarization. Thus substituting Eq. (57) into Eq. (56) will result in R_{total} proportional to the imaginary part of ε_r (i.e. ε_{rI}). At the same time (Shankar, 1994),

$$H^1 = \frac{e}{2mc} \vec{B}_0 \cdot \vec{\mu}_M \tag{58}$$

where $\vec{B}_0$ is the magnetic flux density of the injected light wave; $\vec{\mu}_M$ is the magnetic moment operator of electrons in the material of interest. $\vec{\mu}_M$ represents electrons' angular

momentum which constitutes magnetization. Thus substituting Eq. (58) into Eq. (56) will result in R_{total} proportional to the imaginary part of μ_r (i.e. μ_{rI}).

Because

$$\vec{P}_M \left| \psi_s \right\rangle = 0 \tag{59}$$

Thus according to Eq. (57), the spin part of $\left| \psi_{os} \right\rangle$ and ε_{rI} are irrelative. But $\left| \psi_s \right\rangle$ contains angular momentum and therefore must be involved in μ_{rI}. From Eq. (56) and Eq. (58), we can obtain μ_{rI} as follows:

Applying a spin-orbit decomposition (see Eqs. (53) and (55)) on the kernel of the transition rate expression in Eq. (56) suggests the convenience of defining parameters as follows:

$$\left\langle \psi_{os}^{f0} \left| H^1 \right| \psi_{os}^{i0} \right\rangle = \left(\left\langle \psi_o^{f0} \right| \otimes \left\langle \psi_s^{f0} \right| \right) \cdot H^1 \cdot \left(\left| \psi_o^{i0} \right\rangle \otimes \left| \psi_s^{i0} \right\rangle \right) \equiv t_{total} , \tag{60a}$$

$$\left\langle \psi_o^{f0} \left| H^1 \right| \psi_o^{i0} \right\rangle \equiv t_o , \tag{60b}$$

$$\left\langle \psi_s^{f0} \left| H^1 \right| \psi_s^{i0} \right\rangle \equiv t_s , \tag{60c}$$

where through explicit matrix operations, it can be shown that

$$t_{total} = t_o t_s , \tag{61}$$

As a result, Eq. (56) can be rewritten as:

$$R_{total} = C \cdot \sum_{f,i} t_{os} \cdot \delta \left(E_{os}^{f0} - E_{os}^{i0} - \hbar\omega \right) = C \cdot \sum_{f,i} t_o t_s \cdot \delta \left(E_{os}^{f0} - E_{os}^{i0} - \hbar\omega \right) = R_o \cdot R_s , \tag{62}$$

where

$$R_o = C_o \sum_{f,i} \left| \left\langle \psi_o^{f0} \left| H^1 \right| \psi_o^{i0} \right\rangle \right|^2 \delta \left(E_o^{f0} - E_o^{i0} - \hbar\omega \right) , \tag{63}$$

$$R_s = C_s \sum_{f,i} \left| \left\langle \psi_s^{f0} \left| H^1 \right| \psi_s^{i0} \right\rangle \right|^2 \delta \left(E_s^{f0} - E_s^{i0} - \hbar\omega \right) , \tag{64}$$

with C_o and C_s being constant coefficients.

As aforementioned, despite being termed "electronic transition rate" to account for the lightwave absorption within a material, the primitive transition rate R_{total} is in essence a series of delta functions situated at varying frequencies (or energies, see Eq. (56)), and thus is too spikey to be real. In fact, this spikey nature results from our attempt to describe the dynamics of multitudes of electrons by a limited number of Kohn-Sham orbitals. Therefore, R_{total} ought to be "smoothed" prior to being converted to a realistic absorption spectrum. Here, Gaussian functions are adopted to replace all delta functions. The smoothed R_{total}, R_o and R_s are now denoted as R'_{total}, R'_o and R'_s, respectively, and thus from Eq. (62) we have:

$$R'_{total} = R'_o R'_s , \tag{65}$$

It is a common practice in the first-principle quantum mechanical calculations (such as by the computer codes CASTEP and DMol³ ((Clark et al., 2005), (Delley, 1990)) that R'_o is normally set equal to ε_{rI} simulated with the "spin polarized" option in these kind of codes turned off (as in the nonmagnetic case).

Substituting Eq. (58) into Eq. (64) gives R'_s. And then the product of R'_o and R'_s, R'_{total}, is proportional to μ_{rI} (the scaling factor is defined as C_M). With μ_r being linear and causal, there is an exact one-to-one correspondence between its real and imaginary parts as prescribed by the Kramers-Kronig relation (see, e.g., (Landau & Lifshitz, 1960)). Thus, the real part of μ_r (i.e., μ_{rR}) is readily available once μ_{rI} is numerically obtained. To make all this happen, the calculation of R'_s is now in order.

Within the formulation of R'_s spectrum (see its unsmoothed form in Eq. (64)), physical quantities $\left|\psi_s^{f0}\right\rangle$, $\left|\psi_s^{i0}\right\rangle$, E_s^{f0} and E_s^{i0} would emerge from CASTEP or DMol³ ((Clark et al., 2005), (Delley, 1990)) simulations by selecting the "spin polarized" option. In evaluating the bracketed term in Eq. (64), we first have:

$$t_s \equiv \left\langle \psi_s^{f0} \middle| H^1 \middle| \psi_s^{i0} \right\rangle = \left\langle \psi_s^{f0} \middle| \frac{1}{2} \vec{\mu}_M \cdot \vec{B}_0 \middle| \psi_s^{i0} \right\rangle = \left\langle \psi_s^{f0} \middle| \frac{e}{2mc} \vec{S} \cdot \vec{B}_0 \middle| \psi_s^{i0} \right\rangle , \tag{66}$$

where $\vec{\mu}_M = \gamma \vec{S}$ ($\vec{S}$ being the spin angular momentum), with the gyromagnetic ratio $\gamma = -\frac{ge}{2mc}$ and g = 2 (Shankar, 1994), such that $\frac{e}{2mc}\vec{S} \cdot \vec{B}_0 = \frac{e}{2mc}\left(S_x B_{0x} + S_y B_{0y} + S_z B_{0z}\right)$ in Cartesian coordinate. Further, it is known that the spin angular momentum around the z axis (S_z) (i.e., eigenvectors of $\left|\psi_s^{f0}\right\rangle$ and $\left|\psi_s^{i0}\right\rangle$ possess only two possible eigenvalues: either $+\hbar/2$ (spin up) or $-\hbar/2$ (spin down), with $\hbar$ being the Planck's constant divided by 2π. Hence, the two possible states of $\left|\psi_s^{f0}\right\rangle$ and $\left|\psi_s^{i0}\right\rangle$ expressed on the eigenbasis of S_z are (Shankar, 1994):

Spin up: $\left|\psi_s\right\rangle \leftrightarrow \begin{bmatrix} 1 \\ 0 \end{bmatrix}$, spin down: $\left|\psi_s\right\rangle \leftrightarrow \begin{bmatrix} 0 \\ 1 \end{bmatrix}$, while the spin angular momenta S_x, S_y and S_z are: $S_x \leftrightarrow \frac{\hbar}{2}\begin{bmatrix} 0 & 1 \\ 1 & 0 \end{bmatrix}$, $S_y \leftrightarrow \frac{\hbar}{2}\begin{bmatrix} 0 & -i \\ i & 0 \end{bmatrix}$, $S_z \leftrightarrow \frac{\hbar}{2}\begin{bmatrix} 1 & 0 \\ 0 & -1 \end{bmatrix}$ (Shankar, 1994).

Hence, the value of the bracketed term t_s of Eq. (66) varies according to the four possible combinations of $\left|\psi_s^{f0}\right\rangle$ and $\left|\psi_s^{i0}\right\rangle$, namely:

1. $\left|\psi_s^{f0}\right\rangle$ and $\left|\psi_s^{i0}\right\rangle$ both spin up such that

$$t_s \equiv \left\langle \psi_s^{f0} \middle| \frac{e}{2mc} \vec{S} \cdot \vec{B}_0 \middle| \psi_s^{i0} \right\rangle = \frac{e}{2mc} \left\langle j'm' \middle| S_x B_{0x} + S_y B_{0y} + S_z B_{0z} \middle| jm \right\rangle$$

$$\leftrightarrow \frac{e}{2mc}\begin{bmatrix} 1 & 0 \end{bmatrix}\left(\frac{\hbar B_{0x}}{2}\begin{bmatrix} 0 & 1 \\ 1 & 0 \end{bmatrix} + \frac{\hbar B_{0y}}{2}\begin{bmatrix} 0 & -i \\ i & 0 \end{bmatrix} + \frac{\hbar B_{0z}}{2}\begin{bmatrix} 1 & 0 \\ 0 & -1 \end{bmatrix} \right)\begin{bmatrix} 1 \\ 0 \end{bmatrix} = \frac{e\hbar}{4mc} B_{0z} \equiv t_z$$

2. $\left|\psi_s^{f0}\right\rangle$ spin up, and $\left|\psi_s^{i0}\right\rangle$ spin down such that $t_s = \frac{e\hbar}{4mc}\left(B_{0x} - iB_{0y}\right) \equiv t_{xy}$.
3. $\left|\psi_s^{f0}\right\rangle$ spin down, and $\left|\psi_s^{i0}\right\rangle$ spin up such that $t_s = \frac{e\hbar}{4mc}\left(B_{0x} + iB_{0y}\right) \equiv t_{xy}^{*}$.
4. $\left|\psi_s^{f0}\right\rangle$ and $\left|\psi_s^{i0}\right\rangle$ both spin down such that $t_s = -\frac{e\hbar}{4mc}B_{0z} \equiv -t_z$.

It is obvious that the values of $|t_s|^2$ for cases 1 and 4 are identical, i.e., $|t_z|^2 \equiv T_z$; and those for cases 2 and 3 are the same and are $|t_{xy}|^2 \equiv T_{xy}$.

To simplify the R'_s calculation without loss of generality, the magnetic flux density vector of a linearly polarized electromagnetic wave is oriented to parallel to the z axis, i.e., $\vec{B}_0 = \vec{B}_{0z}$ ($\vec{B}_{0x} = \vec{B}_{0y} = 0$). As a result, only T_z is relevant in the R'_s calculation. Further, as implied by its representation, T_z is invariant in value regardless of what the initial and final energy levels (E_s^{f0} and E_s^{i0}) are in a transition, so long as Fermi's golden rule is satisfied. This property greatly facilitates the calculation of R'_s, in that R'_s now simply becomes proportional to the number of identical-spin transition electron pairs. Within each transition pair there is an energy difference of $\hbar\omega$ while being irradiated by a linearly polarized light of frequency ω.

In first-principle quantum mechanical simulation codes, such as the CASTEP and DMol[3], a finite number of E_s^{f0} and E_s^{i0} are generated to approximate the transitions of a multitude of electrons within a material of interest. In other words, each output energy value actually stands for a narrow continuous band of states centered at this specific value. Therefore, to simulate more closely to the reality, all delta functions of E_s^{f0} and E_s^{i0} are replaced with Gaussian functions prior to being added up into continuous density spectra, for both the "all spin-up" (case 1) and "all spin-down" (case 4) states, respectively. Since the magnetic properties are manifested by unpaired spins, and on the same energy level a spin-up is neutralized by a spin-down (Pauli's exclusion principle), the net spin density spectrum is thus settled by subtracting that of the spin-downs from that of the spin-ups.

With all inner work laid out, the detailed procedure for evaluating R'_s is outlined as follows:

1. Subtract the density spectrum of the spin-down states from that of the spin-ups to result in the net spin density spectrum. The positive part of it is the net spin-up density spectrum, and the absolute value of the other part is the net spin-down density spectrum.
2. Randomly sample the net spin-up density spectrum at each energy of interest and denote the sampled energy value E_i if it is lower than the Fermi level, otherwise, name it E_j.
3. Define $P_{i,j}$, as the product of n_i and n_j, where n_i and n_j are the density-of-states at E_i and E_j, respectively. Namely, $P_{i,j}$ is proportional to the number densities associated with a transition pairs of net spin-up electrons linked by an energy difference of $E_{i,j} \equiv (E_j - E_i)$.
4. Calculate $P_{i,j}$'s and $E_{i,j}$'s for each (E_i, E_j) pair to get the net spin-up $P_{i,j}$ vs. $E_{i,j}$ collection.
5. Obtain the $P_{i,j}$ vs. $E_{i,j}$ collection for the net spin-down states in a similar fashion.
6. Then, obtain the union of the $P_{i,j}$ vs. $E_{i,j}$ collection of the net spin-downs and that of the net spin-ups to result in the total $P_{i,j}$-$E_{i,j}$ collection.
7. Replace all $P_{i,j}$ delta peaks by Gaussian functions to arrive at the desired continuous spectrum of R'_s.

As mentioned, in those cases where the "spin polarized" option in, e.g., CASTEP is turned off, the resultant ε_{rI} spectra actually gives R'_o in Eq. (65). With both R'_s and R'_o being revealed, the optical μ_r spectrum of interest can be secured within a proportional constant C_M, and then the Kramers-Kronig relation. Finally, this universal constant C_M is uncovered by comparing the erected μ_{rI} spectrum with existing data covering from low to lightwave frequencies (Lide & Frederikse, 1994).

The calculated refractive index spectrum of iron crystal from using the proposed approach is shown in Fig. 23. A comparison with the known refractive index spectrum of iron crystal exposed by a linearly polarized light (Lide & Frederikse, 1994) (see Fig. 24) reveals that both figures are relatively close in features. Accordingly, the universal proportional constant C_M obtained from comparing the two N_I curves is about 13.7. The completed iron μ_r spectrum is provided in Fig. 25 after applying $R'_o = \varepsilon_{rI}$, Eq. (66) and then the Kramers-Kronig relation. Therefore, the optical μ_r and refractive index spectra of all materials, including those to be developed, can now be fully explored for the first time.

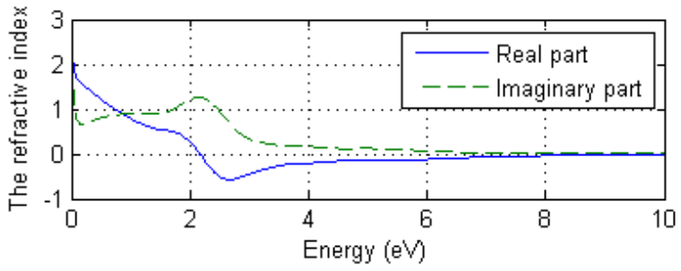

Fig. 23. The calculated relative refractive index spectrum of the Fe crystal (C_M = 1).

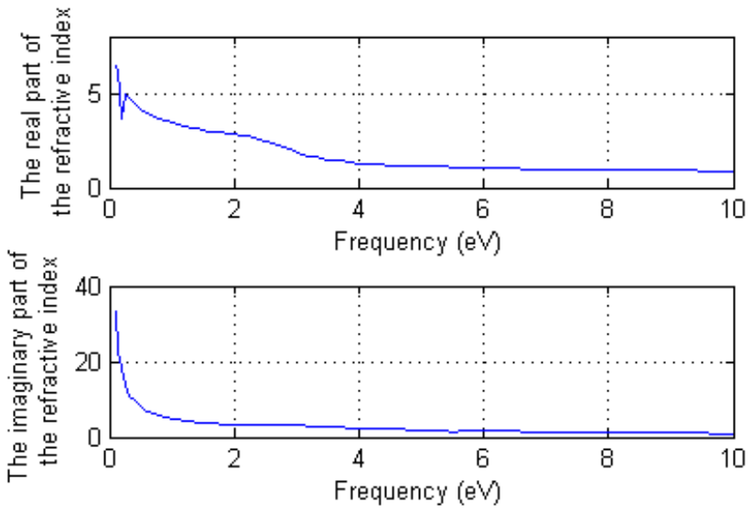

Fig. 24. The refractive index spectrum of Fe crystal in CRC Handbook.

Incidentally, to further challenge the proposed procedure, we erroneously leave the "spin polarized" action of CASTEP on when simulating the copper crystal, a knowingly

nonmagnetic material. It turned out that the numerically converged spin density was a minimal 1.35 x 10^{-4} μ_B/atom, showing that the proposed procedure is robust against erroneous initial conditions.

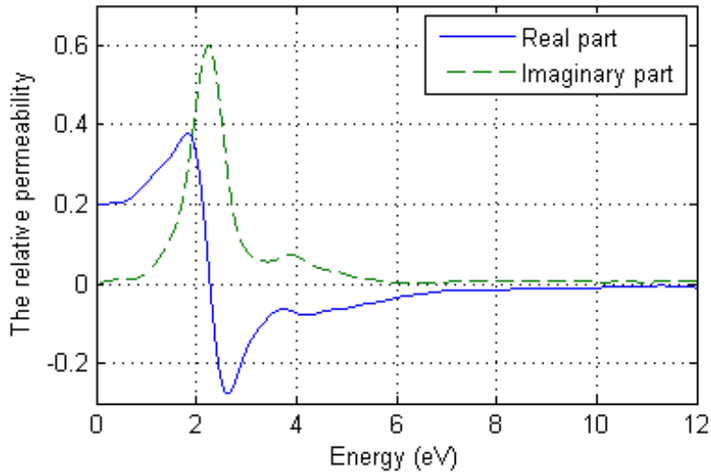

Fig. 25. The optical μ_r spectrum of Fe crystal obtained from the proposed procedure.

10. Conclusion

This chapter contains a clear, yet rigorous, picture as to how the real physical causes behind all these macroscopic optical phenomena – i.e., the microscopic electric and magnetic dipoles-work to come up with such macroscopic results. Both the electric and magnetic dipoles react to the imposed EM wave in such a way that actually results in the Fresnel equations.

In arriving at the more intuitive "scattering form" of the Fresnel equations, microscopic EM-induced physical electric and magnetic dipoles were rigorously employed as the source of electromagnetic waves by Doyle et al. Motivated by such an approach, the authors started to speculate how the incorporation of permanent dipoles might affect many macroscopic optical phenomena, e.g., the Brewster angle of a specific optical material. Among its predictions, the traditionally fixed Brewster angle of a specific material now not only becomes dependent on the density and orientation of incorporated permanent dipoles, but also on the incident light intensity (more precisely, the incident wave electric field strength). Further, two conjugated incident light paths would give rise to different refracted wave powers. This kind of microscopic approaches are called "dipole engineering".

Theoretical elaboration and then IR experiments on poled polyvinylidene fluoride (PVDF) films were conducted to verify the emergence of asymmetric reflections at varying incident angles, as well as the inverse dependence of reflectivity upon the impinging light intensity. In addition, experiments on dipole-engineered PVDF films show that by way of adding/reducing permanent dipole density and varying orientations, the aforementioned theoretical predictions can be evidenced unambiguously in the visible light range. Further, effective polarization density can be quantified from the above experiments subjected to different dipole engineering processes. As a result, the traditionally elliptic contour of a slanted two dimensional section of the refractive index ellipsoid now manifests symmetric

open splittings at near the traditional incident angle. It implies that severe challenge to the accuracy of traditional surface plasmon resonance measurements may arise in the presence of permanent dipoles of various morphologies, such as in the forms of nano-particles or membrane double layers.

Traditional approach of obtaining electric permittivity through directly measuring a material's refractive index begins to appear flawed at dawn of the nanotech era. On the other hand, achieving novel magnetics and thus new materials of variable refractive indices starts to become meaningful. However, unlike its electric counterpart, data for optical magnetic permeability is hardly available for most materials. An effective method is proposed to secure practically accurate optical permeabilities through manipulating electronic transition rates generated by first-principle quantum mechanical simulations.

11. References

Alex J. Goldman. (1999). *Handbook of Modern Ferromagnetic Materials*, Springer, Kluwer Academic Publishers, Norwell, MA. (Goldman, 1999)

B. Alberts, A. Johnson, J. Lewis, M. Raff, K. Roberts. (2007). *Molecular Biology of the Cell*, Garland Science, New York. (Alberts et al., 2007)

B. Delley. (1990). "An all–electron numerical method for solving the local density functional for polyatomic molecules", *The Journal of Chemical Physics*, vol. 92, (1990), 508. (Delley, 1990)

Chungpin Liao, Hsien-Ming Chang, and Chien-Jung Liao. (2006). "Manipulating the Brewster angles by using microscopically coherent dipole quanta and its possible implications," *IEEE Journal Lightwave Technology*, vol. 24, no. 8, (Aug 2006), pp. 3248-3254. (Liao et al., 2006)

D. A. G. Bruggeman. (1935). „Berechnung verschiedener physi-kalischer Konstanten von heterogenen Substanzen. I. Di-elektrizitätskonstanten und Leitfähigkeiten der Mischkörper aus isotropen Substanzen", *Annalen der Physik*, vol. 416, (1935), pp. 665-679. (Bruggeman, 1935)

D. R. Lide, H. P. R. Frederikse. (1994). *CRC Handbook of Chemistry and Physics*, pp.123-124, CRC-Press, Boca Raton, FL. (Lide & Frederikse, 1994)

David K. Cheng. (1989). *Field and Wave Electromagnetics*, second ed., Addison-Wesley Pub. Co., Reading, MA. (Cheng, 1989)

E. Hecht. (2002). *Optics*, 4th Ed., Addison Wesley, New York. (Hecht, 2002)

Edward M. Purcell. (1985). *Electricity and Magnetism*, 2nd Ed., Education Development Center, Inc., MA. (Purcell, 1985)

Finn Jorgensen. (1995). *The Complete Handbook of Magnetic Recording*, McGraw-Hill, New York. (Jorgensen, 1995)

H. A. Haus and J. R. Melcher. (1989). *Electromagnetic Fields and Energy*, Prentice-Hall, New York. (Haus & Melcher, 1989)

H. A. Lorentz. (1880). „Ueber die Beziehung zwischen der Fortpflanzungsgeschwindigkeit des Lichtes und der Körperdichte", *Annalen der Physik*, vol. 9, (1880), pp. 641-665. (Lorentz, 1880)

H. Raether. (1988). "Surface Plasmons on Smooth and Rough Surfaces and on Gratings," In: *Springer Tracts in Modern Physics*, Springer, Berlin. (Raether, 1988)

Hsien-Ming Chang and Chungpin Liao. (2011). "A Parallel Derivation to the Maxwell-Garnett Formula for the Magnetic Permeability of Mixed Materials", *World Journal of Condensed Matter Physics*, in press. (Chang & Liao, 2011)

J. C. Maxwell Garnett. (1904). “Colours in Metal Glasses and in Metallic Films”, *Philosophical Transactions of the Royal Society of London*. Series A, Containing Papers of a Mathematical or Physical Character, vol. 203, (1904), pp. 385-420. (Garnett, 1904)

Jun-Lang Chen, Min-Yen Shieh, Hsin Her Yu, Chungpin Liao, Hsien-Ming Chang, Bin-Huang Yang, and Zi-Peng Zhao. (2008). "Asymmetric reflectivity from surfaces with distributed dipoles and IR experiments on poled polyvinylidene difluoride films", *APPLIED PHYSICS LETTERS*, vol. 93, 011902, (July 2008). (Chen et al., 2008)

K.M. Yassien, M. Agour, C. von Kopylow and H.M. EI-Dessouky. (2010). “On the digital holographic interferometry of fibrous material, I: Optical properties of polymer and optical fibers,” *Optics and Lasers in Engineering* , Vol. 48, Issue 5, (2010), pp. 555-560. (Yassien et al., 2010)

L. Lorenz. (1880). „Ueber die Refractionsconstante“, *Annalen der Physik*, Vol. 11, (1880), pp. 70-103. (Lorenz, 1880)

L.D. Landau, E.M. Lifshitz. (1960). *Electrodynamics of Continuous Media*, pp. 260-263, Pergamon Press, Oxford. (Landau & Lifshitz, 1960)

M. Matsukawa, K. Shintani, S. Tomohiro and N. Ohtori. (2006). “Application of Brillouin scattering to the local anisotropy and birefringence measurements of thin layers,” *Ultrasonics*, Vol.44, Suppl. 1, (2006), pp. e1555-e1559. (Matsukawa et al., 2006)

P. W. Atkins and R. S. Friedman. (1997). *Molecular quantum mechanics*, Oxford University Press, New York. (Atkins & Friedman, 1997)

Paul Lorrain, Dale R. Corson. (1970). *Electromagnetic Fields and Waves*, second ed., W.H.Freeman & Co Ltd, San Francisco. (Lorrain & Corson, 1970)

Po-Yu Tsai, Chien-Jung Liao, Wen-Kai Kuo, Chungpin Liao. (2011). "Birefringence caused by the presence of permanent dipoles and its possible threat on the accuracy of traditional surface plasmon", *World Journal of Condensed Matter Physics*, in press. (Tsai et al., 2011)

Pramoda K. Pallathadka. (2006). “Solid state ^{19}F NMR study of crystal transformation in PVDF and its nanocomposites (polyvinylidene fluoride)”, *Polymer Engineering and Science*, 46(12), 1684-7, (2006). (Pallathadka, 2006)

Q. M. Zhang, V. Bharti, G. Kavarnos. (2002). "Poly (Vinylidene Fluoride) (PVDF) and its Copolymers", In: Encyclopedia of Smart Materials, M. Schwartz (Ed.), Volumes 1-2, pp. 807-825, John Wiley & Sons, and references therein. (Zhang et al., 2002)

R. Shankar. (1994). *Principles of Quantum Mechanics*, Springer Science & Business Media, New York. (Shankar, 1994)

Rolf E. Hummel. (1985). *Electronic Properties of Materials*, pp. 243-247, Springer-Verlag, New York. (Hummel, 1985)

S. A. Maier. (2007). *Plasmonics: Fundamental and Applications*, Springer, New York. (Maier, 2007)

Stewart J. Clark, M.D. Segall, Christopher J Pickard, P.J. Hasnip, M. I. J. Probert, Keith Refson, and Mike C. Payne. (2005). "First principles methods using CASTEP", *Zeitschrift Fuer Kristallographie*, vol. 220, (2005), pp. 567-570. (Clark et al., 2005)

W. Lamb, D. M. Wood, and N. W. Ashcroft. (1980). “Long-wavelength electromagnetic propagation in heterogeneous media”, *Physical Review B*, vol. 21, no. 6, (March 1980), pp. 2248-2266. (Lamb et al., 1980)

W. T. Doyle. (1985). “Scattering approach to Fresnel’s equations and Brewster’s law,” *Am. J. Phys.*, 53 (5), pp. 463-468. (Doyle, 1985)

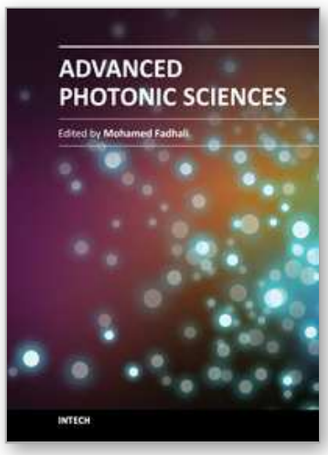

Advanced Photonic Sciences

Edited by Dr. Mohamed Fadhali

ISBN 978-953-51-0153-6
Hard cover, 374 pages
Publisher InTech
Published online 21, March, 2012
Published in print edition March, 2012

The new emerging field of photonics has significantly attracted the interest of many societies, professionals and researchers around the world. The great importance of this field is due to its applicability and possible utilization in almost all scientific and industrial areas. This book presents some advanced research topics in photonics. It consists of 16 chapters organized into three sections: Integrated Photonics, Photonic Materials and Photonic Applications. It can be said that this book is a good contribution for paving the way for further innovations in photonic technology. The chapters have been written and reviewed by well-experienced researchers in their fields. In their contributions they demonstrated the most profound knowledge and expertise for interested individuals in this expanding field. The book will be a good reference for experienced professionals, academics and researchers as well as young researchers only starting their carrier in this field.

How to reference

In order to correctly reference this scholarly work, feel free to copy and paste the following:

Chungpin Liao, Hsien-Ming Chang, Chien-Jung Liao, Jun-Lang Chen and Po-Yu Tsai (2012). Lightwave Refraction and Its Consequences: A Viewpoint of Microscopic Quantum Scatterings by Electric and Magnetic Dipoles, Advanced Photonic Sciences, Dr. Mohamed Fadhali (Ed.), ISBN: 978-953-51-0153-6, InTech, Available from: http://www.intechopen.com/books/advanced-photonic-sciences/lightwave-refraction-and-its-consequences-a-viewpoint-microscopic-quantum-scatterings-by-electric-an

INTECH
open science | open minds

InTech Europe
University Campus STeP Ri
Slavka Krautzeka 83/A
51000 Rijeka, Croatia
Phone: +385 (51) 770 447
Fax: +385 (51) 686 166
www.intechopen.com

InTech China
Unit 405, Office Block, Hotel Equatorial Shanghai
No.65, Yan An Road (West), Shanghai, 200040, China
中国上海市延安西路65号上海国际贵都大饭店办公楼405单元
Phone: +86-21-62489820
Fax: +86-21-62489821

© 2012 The Author(s). Licensee IntechOpen. This is an open access article distributed under the terms of the Creative Commons Attribution 3.0 License, which permits unrestricted use, distribution, and reproduction in any medium, provided the original work is properly cited.

IntechOpen

IntechOpen